energies

Article

Development and Experimental Field Validation of an Arduino-Based Condition Monitoring System for Heliostat Drive Units †

Dominik Steinberg [1,2,*], Stefan Nicolas Huestegge [1,‡], Daniel Maldonado Quinto [3], Marc Röger [4], Benedikt Kölsch [3] and Robert Pitz-Paal [2,3]

[1] Institute of Solar Research, German Aerospace Center (DLR), Im Langenbroich 13, 52428 Jülich, Germany
[2] Chair of Solar Technology (DLR), RWTH Aachen University, Linder Höhe, 51147 Cologne, Germany
[3] Institute of Solar Research, German Aerospace Center (DLR), Linder Höhe, 51147 Cologne, Germany
[4] Institute of Solar Research, German Aerospace Center (DLR), Calle Doctor Carracido 44, 04005 Almería, Spain
* Correspondence: dominik.steinberg@dlr.de
† This paper is an extended version of our paper published: Steinberg, D.; Huestegge, S.N.; Maldonado Quinto, D.; Röger, M.; Kölsch, B.; Pitz-Paal, R. Cost-Efficient Prognostics Framework for Heliostat Drive Units. *Proc. Eur. Conf. PHM Soc.* **2026**, *9*, 1–17. https://doi.org/10.36001/phme.2026.v9i1.4955.
‡ Stefan Nicolas Huestegge worked formerly at affiliation 1.

Abstract

In concentrating solar power tower plants, heliostat drive units (HDUs) are critical components that control the precise two-axis alignment of the heliostats focussing solar radiation onto the receiver. Consequently, the reliable operation of HDUs is essential for safe and stable plant operation. However, existing research on heliostat operation and maintenance (O&M) predominantly focuses on aspects such as soiling, calibration, and the influence of wind loads on heliostat behaviour. In contrast, the operational health of HDUs remains largely unexplored. Addressing this research gap, this study develops a cost-efficient Arduino-based condition monitoring system (ACMS) measuring vibration and magnetic flux density signals of the HDUs. The field validation is conducted at the DLR solar tower research facility in Jülich, Germany (STJ). By this, the high measurement stability and reliability of the ACMS (>99.9% data availability during a 24 h stationary outdoor test measurement) is demonstrated. Thus, the ACMS provides a reliable basis for detecting HDU condition-sensitive changes in the recorded operational data. For example, the ACMS captures an unexpectedly pronounced increase in HDU vibration amplitude during comparable HDU operational movements, reaching approximately ten times the previously observed nominal level. While the underlying cause cannot yet be conclusively identified, this demonstrates the potential of the ACMS to detect emerging abnormal HDU behaviour. Overall, the chosen cost-efficient approach provides a scalable basis for HDU condition monitoring, supporting efforts to enhance heliostat reliability within O&M processes.

Keywords: concentrating solar technologies; heliostat drive unit; operation and maintenance; condition monitoring; anomaly detection; low-cost sensing; vibration analysis; magnetic field analysis

Check for updates

Academic Editors: Chuncheng Zang, Antonio Rosato and Giovanna Pallotta

Received: 27 August 2026
Revised: 22 September 2026
Accepted: 23 September 2026
Published: 28 September 2026

Copyright: © 2026 by the authors. Licensee MDPI, Basel, Switzerland. This article is an open access article distributed under the terms and conditions of the Creative Commons Attribution (CC BY) license.

1. Introduction

Within concentrating solar technologies (CST), solar power tower plants are an important technology in which large heliostat fields act as solar collectors by reflecting the incoming solar radiation onto a central receiver mounted on top of a tower. By this, thermal

energy is generated that can subsequently be converted into electricity. Alternatively, the thermal energy can be used for high-temperature industrial process heat, or can be applied in thermochemical processes. As shown in Figure 1, each heliostat typically consists of

- mirror facets that reflect the incoming sunlight,
- a support structure maintaining the prescribed position and orientation of the mirror facets to limit slope errors and preserve optical accuracy,
- a pylon-foundation system providing structural stability and ground connection, and heliostat drive units (HDUs) that actuate the heliostat to enable continuous two-axis sun tracking by accurately orienting the mirror facets towards the receiver [1–4].

Due to the large heliostat–receiver distances L occurring in practice, even small angular deviations $\Delta\alpha$ can lead to significant (and thus, operationally undesirable) beam displacements Δy on the receiver. For example, a deviation $\Delta\alpha$ of the mirror facet normal causes a $2\Delta\alpha$ deviation of the reflected beam, yielding $\Delta y = L\tan(2\Delta\alpha)$. Hence, for $L = 1\,\text{km}$, $\Delta\alpha = 1\,\text{mrad}$ ($\approx 0.057°$) results in beam displacements of approximately 2 m.

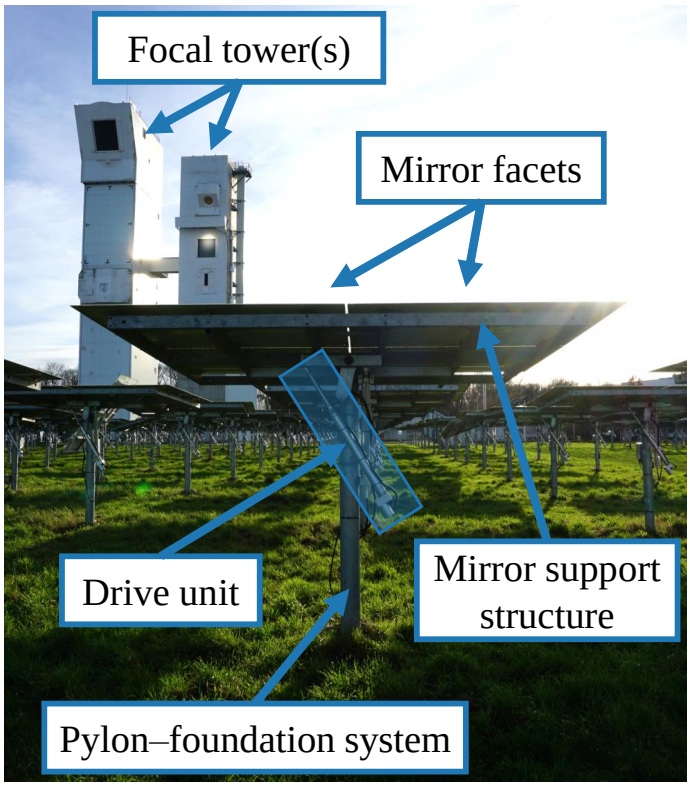


Figure 1. Heliostat field at the DLR solar tower research facility in Jülich, Germany (STJ). The receivers on the top of both focal towers are visible in the background.

The operational reliability of HDUs is therefore crucial for the overall performance of solar tower plants. Failures of HDU components can lead to considerable maintenance efforts and reduced plant availability, while additionally, misdirected solar radiation due to heliostat actuation errors may pose operational and safety risks. Due to the large distances between the heliostat and the receiver, even small angular deviations in the heliostat's orientation within the milliradian range can result in significant focal point displacement at the receiver.

Modern heliostat fields usually consist of between 10^3–10^5 heliostats, each equipped with two HDUs corresponding to the two rotational axes required for continuous sun tracking. In the context of this work, the terms *heliostat axis* and the corresponding *HDU*

are used synonymously. This means that investigating a given *axis* refers to the HDU responsible for actuating motion along that axis.

From an operation and maintenance (O&M) perspective, HDUs represent a highly critical subsystem for reliable and safe solar tower plant operation. However, maintenance strategies in heliostat fields have traditionally relied on reactive or preventive approaches only. Reactive maintenance reacts to failures after they occur, often causing unexpected downtime, whereas preventive maintenance schedules component replacement at predefined intervals, which frequently leads to unnecessary interventions. In contrast, condition-based and predictive maintenance strategies are designed to monitor the actual operational state of components or subsystems, thereby enabling deviations from normal behaviour to be detected at an early stage [5–7].

The large number of heliostats in utility-scale plants represents a key challenge for the development of such advanced monitoring solutions for HDUs, necessitating technically robust, economically scalable, and easily deployable monitoring approaches. This motivates using cost-efficient and non-intrusive sensing concepts that can be integrated with minimal installation effort. Low-cost sensors offer several advantages compared to conventional industrial-grade monitoring equipment, including significantly lower hardware costs, smaller size, reduced weight, and lower power consumption. Combined with low-cost microcontroller platforms, these sensing solutions enable scalable monitoring architectures aligned with Industry 4.0 paradigms. These paradigms include IoT connectivity, big data analytics, and predictive maintenance strategies [8–10].

Despite these developments regarding cost-efficient sensing concepts in other research and application fields, experimental investigations of such concepts for HDUs are largely absent, particularly under realistic field operating conditions. Thus, the practical applicability and diagnostic potential of cost-efficient sensing approaches for heliostat condition monitoring have so far received only very limited systematic investigation. To address this gap, the present study develops and experimentally validates a cost-efficient Arduino-based condition monitoring system (ACMS) for monitoring HDUs. In this context, the present study conducts a dedicated field measurement campaign at the DLR solar tower research facility in Jülich, Germany (STJ). In addition, the proposed ACMS approach is assessed through qualitative and semi-quantitative comparisons with conventional industrial-grade sensing hardware.

2. State of the Art and Related Research

The relevant literature is reviewed from three complementary perspectives: the techno-economic basis of condition monitoring and data-driven maintenance (cf. Section 2.1), condition monitoring in heliostat fields (cf. Section 2.2), and cost-efficient sensing architectures for data acquisition (cf. Section 2.2).

2.1. Existing Research on the Techno-Economic Foundations of Condition Monitoring and Data-Driven Maintenance Strategies

When machines must remain fully operational and available “24/7”, it becomes imperative to detect potential disruptions, failures, or damages at an early stage. This early detection enables the timely implementation of corrective measures. Thereby, the risk of an unexpected downtime or complete system failures, which could otherwise result in significant economic losses [11,12], is minimised. The decision made by the machine owner and/or machine operator to implement a condition monitoring system should be guided by a thorough cost assessment, weighing the potential savings against the investment costs of the system [12].

In 2025, the global market volume for machine condition monitoring amounted to around 3.8 billion US dollars. Moreover, the global market volume is forecasted to grow at a compound annual growth rate (CAGR; geometric mean annual growth rate) of 7.0% from 2026 to 2033 [9,13]. However, it was found that most of the literature on condition monitoring focuses on diagnostic and prognostic methods as well as optimisation models. In contrast, there are only a few approaches in the literature for the (practically validated) implementation of condition monitoring [14].

Over the past few years, the increasing complexity of machines and the criticality of reliability and availability, together with the rise of digitalisation and connectivity, have changed the industry as a whole. These developments have also shaped the evolution of maintenance strategies [9,12,15,16] as summarised in Figure 2 and outlined below.

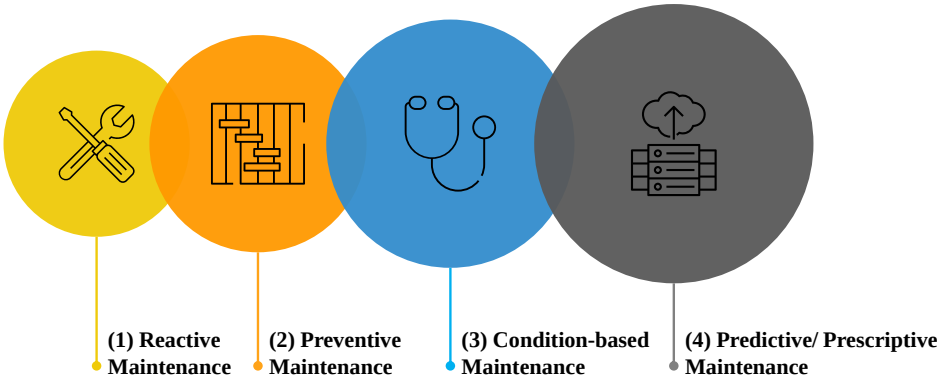


Figure 2. Evolution of maintenance strategies (adapted from [15]). The chronological development proceeds from left to right. Larger circles represent more recent maintenance strategies with increasing methodological and technological complexity.

- Maintenance 1.0: *Reactive maintenance* (also called *corrective maintenance* [15] or *breakdown maintenance* [11]) involves addressing faults only after they have occurred, focusing on restoring functionality rather than preventing failures [15].
- Maintenance 2.0: *Preventive maintenance* (also called *planned maintenance* [11]) aims to reduce the likelihood of failures by performing routine checks based on predetermined (periodic) time schedules or usage schedules [15,17].
- Maintenance 3.0: *Condition-based maintenance* relies on monitoring the condition of equipment to identify potential issues and initiate repairs only when necessary, rather than adhering to a fixed maintenance schedule [15].
- Maintenance 4.0: *Predictive maintenance* uses real-time sensor data as well as sophisticated algorithms and advanced analytics, including fuzzy logic, machine learning and probabilistic reasoning, to anticipate and predict failures before they occur [12,15]. *Prescriptive maintenance* (also called *smart maintenance* or *proactive maintenance* [9,15,16]) extends beyond the capabilities of *predictive maintenance*. In addition to forecasting potential failures, it provides precise and actionable recommendations to proactively prevent them and addresses the question of how to control the occurrence of a specific event [15,18].

In the context of this paper, the transition between Maintenance 3.0 and Maintenance 4.0 paradigms is regarded as seamless, as also done in [11]. Thus, the term "condition monitoring" is used to refer to both maintenance strategies.

With the development of more advanced maintenance strategies (cf. Figure 2), data has become increasingly important. The way in which data is handled has evolved in a variety of ways, including data sources, data collection methods, data storage and data management [15]. During the era of Maintenance 1.0, data largely stemmed from

operator experience, which remained neither documented nor analysed. Over time, however, formal documentation and databases emerged, data collection processes became progressively automated, and data sources expanded (e.g., through the deployment of sensors). These developments ultimately led to "data-driven" (e.g., statistics-based, pattern recognition-based, AI-based [19]) maintenance strategies. This means that processes and workflows are both based on and shaped by the operational data of the monitored machine/equipment [10,11,15]. According to [15], data constitutes the key component of intelligent maintenance. Therefore, when examining the role of data in modern maintenance strategies, it becomes clear that data-driven insights are no longer just supplementary, but integral.

2.2. Existing Research on Heliostat Field Condition Monitoring

A review of the literature on condition monitoring or O&M of heliostat fields indicates that the mechanical subsystem of the HDUs is generally not considered explicitly in existing studies. Instead, the literature predominantly addresses optical performance, environmental influences affecting heliostat mirrors, and methods aimed at improving heliostat tracking accuracy and calibration.

In particular, many studies examine the effects and the mitigation of soiling, which describes the accumulation of dust and sand on reflective surfaces and which can lead to reflectivity degradation and reduced optical efficiency [20–23]. Another major research direction concerns wind-induced effects, focusing on aerodynamic loading and the resulting structural response of heliostats [24–27]. Furthermore, considerable research efforts have addressed tracking accuracy and calibration, aiming to minimise optical alignment errors through improved control strategies, calibration procedures as well as image-based measurement approaches [28–32]. In contrast, comparatively little research has addressed the O&M of HDUs. In particular, sensor-based condition monitoring of the HDU key components such as the electric motors, gearboxes, or ball-screw mechanisms remains under-explored in the peer-reviewed literature. Furthermore, to the best of the authors' knowledge, publicly available time-series datasets capturing the operational behaviour of HDUs are currently lacking. This absence significantly constrains the development, benchmarking, and validation of data-driven condition monitoring approaches. Consequently, there is a clear research gap regarding sensor-based monitoring methodologies capable of detecting deviations in the operational behaviour of HDUs under real field conditions.

2.3. Existing Research on Cost-Efficient Sensing Architectures for Data Acquisition

In many applications, condition monitoring relies on industrial-grade sensing hardware and data acquisition platforms that offer high accuracy, robustness, and reliability. However, their comparatively high acquisition, installation, and operating costs often limit deployment to only a small number of critical assets, thereby constraining large-scale monitoring in cost-sensitive industrial environments [33–35].

To address this limitation, extensive research has explored cost-efficient monitoring options based on low-cost sensors, microcontrollers, and Internet-of-Things (IoT) platforms, including resource-constrained hardware systems, e.g., Arduino, or Raspberry Pi [34,36–38]. In particular, numerous studies have demonstrated the feasibility of vibration- and acoustic-based condition monitoring systems implemented on such resource-constrained hardware platforms, often combined with micro-electromechanical system (MEMS) sensors [39–44]. Such cost-efficient monitoring approaches have also been successfully applied in various technical monitoring domains including rotating machinery [45], manufacturing processes, industrial equipment monitoring and renewable energy systems such as photovoltaic (PV) power plants [46,47]. However, the monitored (i.e., measured) quantities differ considerably

between these application domains: For e.g., rotating machinery, the studies reviewed in [45] focus, among others, on vibration and acceleration data, acoustic emission data, torsional vibration data, and combinations of vibration data with motor current data. In contrast, the PV monitoring studies [46,47] focus on electrical quantities, e.g., voltage, current and power data (from the PV arrays, batteries, and inverters) as well as on environmental quantities, e.g., panel and ambient temperature and solar irradiance.

Despite these developments in other domains, the application of low-cost sensing architectures to HDUs has, to the best of the authors' knowledge, not yet been investigated in the literature. However, the proven effectiveness of these approaches for other monitoring applications provides strong motivation for investigating their applicability to HDU monitoring under real field conditions.

3. Methodology

To address the research gaps identified in Section 2, this study considers the economic potential of modern, particularly data-driven, maintenance strategies beyond conventional reactive and preventive approaches. Accordingly, a dedicated field measurement campaign is conducted using a custom-built, cost-efficient Arduino-based condition monitoring system (ACMS).

The objective of the measurement campaign is to investigate the cost-efficient monitoring of HDUs and to derive diagnostic information from operational sensor signals. For this purpose, and motivated by the use of mechanical (e.g., vibration) and electromagnetic (e.g., motor current) quantities in related condition monitoring applications (cf. Section 2), vibration data and magnetic flux density data are acquired directly at the HDUs during operation.

The underlying working hypothesis is that these two quantities are complementary indicators of the HDU condition: vibration primarily reflects the mechanical behaviour of the HDUs, while magnetic flux density provides a non-invasive measure associated with the electromagnetic behaviour of the motor.

Motor temperature is not considered a primary condition indicator in the present study because the temperature increases caused by the short, intermittent heliostat movements are assumed to be small compared with variations in ambient temperature. This assumption is supported by preliminary tests conducted prior to the actual measurement campaign.

As illustrated in Figure 3, the HDUs convert the rotational motion of the electric motor into linear motion via a gearbox and a ball-screw mechanism. Monitoring the dynamic behaviour of these components during operation therefore provides valuable information about the mechanical condition of the drive unit. The methodology developed in this study comprises three main elements:

- The design of a cost-efficient measurement system,
- the experimental design for data acquisition during the field measurement campaign, and the subsequent data analysis and evaluation of the recorded signals.

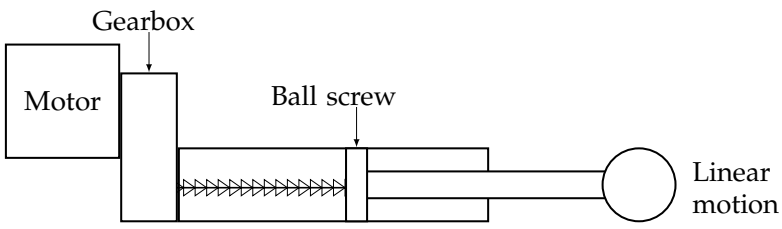


Figure 3. Functional schematic of a heliostat drive unit (HDU) as used at the STJ.

3.1. Measurement System

The proposed ACMS comprises an Arduino-based data acquisition architecture which is depicted in Figure 4a: In brief, analogue sensor signals are either routed directly to the Arduino microcontroller or passed through an optional analogue signal conditioning stage before digitisation. The digitised data are subsequently transmitted to the measurement computer or, alternatively, stored on a USB device. For this work, an Arduino GIGA R1 WiFi (Arduino S.r.l., Monza, Italy) is used (cf. Figure 4b), which is based on the STM32H747XI microcontroller (STMicroelectronics, Geneva, Switzerland) [48].

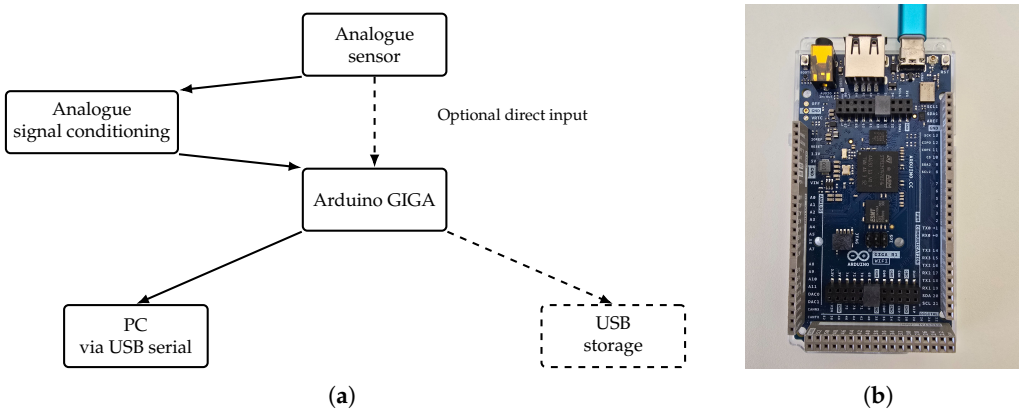


Figure 4. Illustration of the Arduino-based condition monitoring system (ACMS). (**a**) Functional schematic of the ACMS. (**b**) Photograph of the Arduino GIGA R1 WiFi used for this work.

3.1.1. Sensor Selection and Rationale

For each HDU, two analogue sensors are installed: one Hall-effect sensor (providing 1 measurement value) and one MEMS-based 3-axis accelerometer (providing 3 measurement values). Consequently, a total of four (eight) sensor channels are recorded per HDU (per heliostat). Digital sensors are deliberately not employed in the present setup, as they typically impose limitations on the achievable stable sampling rate f_{chosen} (cf. Section 3.1.2). This is because most digital sensors communicate with the Arduino via the Inter-Integrated Circuit (I^2C) interface which is a serial communication bus using two lines: SCL (serial clock) and SDA (serial data). Preliminary experiments performed during this study confirmed that I^2C-connected sensors require approximately one order of magnitude more time for data acquisition T_{readout} than directly sampled analogue sensors: The typical readout times are $T_{\text{readout}} \approx 1000\,\mu\text{s}$ and $T_{\text{readout}} \approx 100\,\mu\text{s}$, respectively. Nevertheless, the Arduino-based data acquisition architecture would in principle also allow for the integration of digital sensors if required.

3.1.2. Data Acquisition and Logging Architecture

The achievable maximum data sampling rate f_{max} depends on the number and type of connected sensors (i.e., digital or analogue sensors) as well as on the stability of the data transmission. Therefore, extensive preliminary experiments have been conducted to determine stable data logging operating conditions. The empirically derived Equation (1) describes an upper limit for the selected sampling rate f_{chosen} as

$$f_{\text{chosen}} \overset{!}{\leq} \frac{1}{T_{\text{readout}} \cdot \gamma} = \frac{1}{(n \cdot m \cdot 9\,\mu\text{s} + 100\,\mu\text{s}) \cdot \gamma}, \tag{1}$$

depending on the number of analogue sensor channels n, the averaging factor m (cf. Section 3.1.3), and a conservative margin factor $\gamma \geq 1$ introduced to account for additional timing uncertainties.

For a single sensor channel ($n = 1, m = 1$), a maximum stable sampling rate of approximately $f_{max} \approx 7.65\,\text{kHz}$ can be achieved. For the monitoring of one heliostat (i.e., $n = 8$, cf. Section 3.1.1) using $m = 8$ and $\gamma = 1.2$, Equation (1) yields $f_{chosen} \overset{!}{\leq} 1.2\,\text{kHz}$.

For the ACMS, it was decided that the sensor signals are sampled at a rate of

$$f_{chosen} = 1.0\,\text{kHz}\,. \tag{2}$$

Thus, the selected sampling rate of $f_{chosen} = 1\,\text{kHz}$ is considered appropriate for the specific monitoring objectives of this study. f_{chosen} remains below the calculated multi-channel sampling limit and retains a performance margin for stable continuous acquisition and future extensions.

During the heliostat operation, the sensor data are continuously streamed via USB serial communication to a measurement computer as shown in Figure 4a. Each received data packet is assigned a UNIX timestamp. For the efficient handling of larger datasets, the data are stored in HDF5 format. This format provides a highly efficient, structured container for large time-series datasets. Moreover, basic consistency checks are performed and potential transmission errors are handled by the developed custom Python-based (Python version 3.10.6) logging and storing script. In addition, each measurement is subject to manual metadata management, which involves documenting relevant environmental conditions, experimental parameters and noteworthy observations during operation.

In a final processing step, the raw digital sensor readings are converted into physical quantities. The analogue-to-digital converter (ADC) values are first converted into voltages, which are then mapped to the corresponding physical units using the sensor-specific calibration parameters (offset and sensitivity). For all sensors, additional calibration measurements were performed to improve measurement accuracy.

3.1.3. Analogue Signal Conditioning, ADC Resolution and Measurement Uncertainty

To utilise the input range of the Arduino ADC $U_{ADC,range}$ (cf. Equation (8)) as efficiently as possible, an analogue signal conditioning stage is implemented. As described in Appendix A.1, this analogue signal conditioning stage comprises three main components: a first-order RC high-pass filter, a voltage divider and a non-inverting amplifier.

Based on targeted control experiments, the uncertainty of the overall measurement chain is considered sufficiently low for the intended analyses in the context of this work. A detailed description of the ADC resolution and the measurement uncertainty of the ACMS is provided in Appendix A.2.

3.2. Experimental Setup

The experimental design is structured to enable comparative measurements under reproducible operating conditions, both across different heliostats and for the same heliostat at different points in time. This provides the basis for identifying relative changes in the recorded operational signals (cf. Section 3.3).

3.2.1. Controlled Heliostat Movement Sequences

In the above mentioned context, the signals (e.g., vibration signals) are only meaningful while the corresponding heliostat axis is in motion. Therefore, the experiments necessitate controlled movement sequences implemented using dedicated control software. For example, such a movement sequence may consist of the periodic extension and retraction of one of the two axes by a predefined number of 15,000 actuator steps, for instance. Another representative sequence consisting of nine single movement steps is presented in Figure 5.

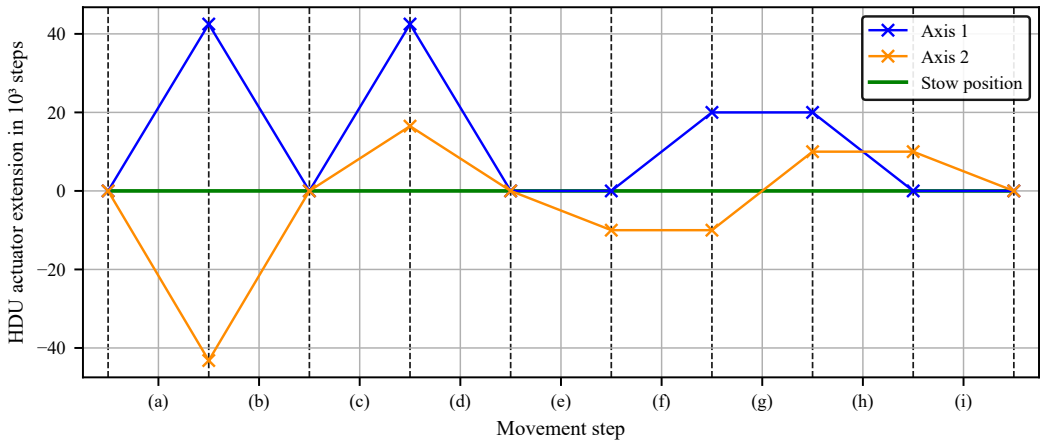


Figure 5. Relative HDU actuator extensions for Axis 1 and Axis 2 during the nine-step movement sequence (a–i), referenced to the stow position. The vertical dashed lines mark the boundaries between consecutive movement steps. The horizontal green line indicates the stow position, i.e., the heliostat is in stow when both curves (blue: Axis 1 and orange: Axis 2) lie on this line simultaneously. Each plotted value on these two curves represents the cumulative actuator extension relative to the stow position. It should be noted that, for the heliostats within the heliostat field of the STJ considered here, the stow position is asymmetric in the actuator phase space: Axis 1 is approximately fully retracted in stow, whereas Axis 2 is approximately half extended. Consequently, the movement sequence exhibits a pronounced asymmetry between both axes.

Since all measurements are intended for comparative analysis, each experiment and its repetitions are conducted using the same predefined movement sequence. This ensures consistent and reproducible experimental conditions, while also accounting for the significant impact of the extension and retraction states of both axes on the measured vibration response.

3.2.2. Measurement Campaign

Data were collected during an eight-month measurement campaign, from July 2025 to February 2026, in the heliostat field of the STJ (cf. Figure 1) which comprises more than 2000 heliostats [49]. For the present study, a group of eight neighbouring heliostats is selected without prior screening with respect to the experimental objectives. Both HDUs of each selected heliostat are instrumented. The IDs of these eight neighbouring heliostats are:

$$12023, 12024, 12025, 12026, 12123, 12124, 12125, \text{and } 12126. \quad (3)$$

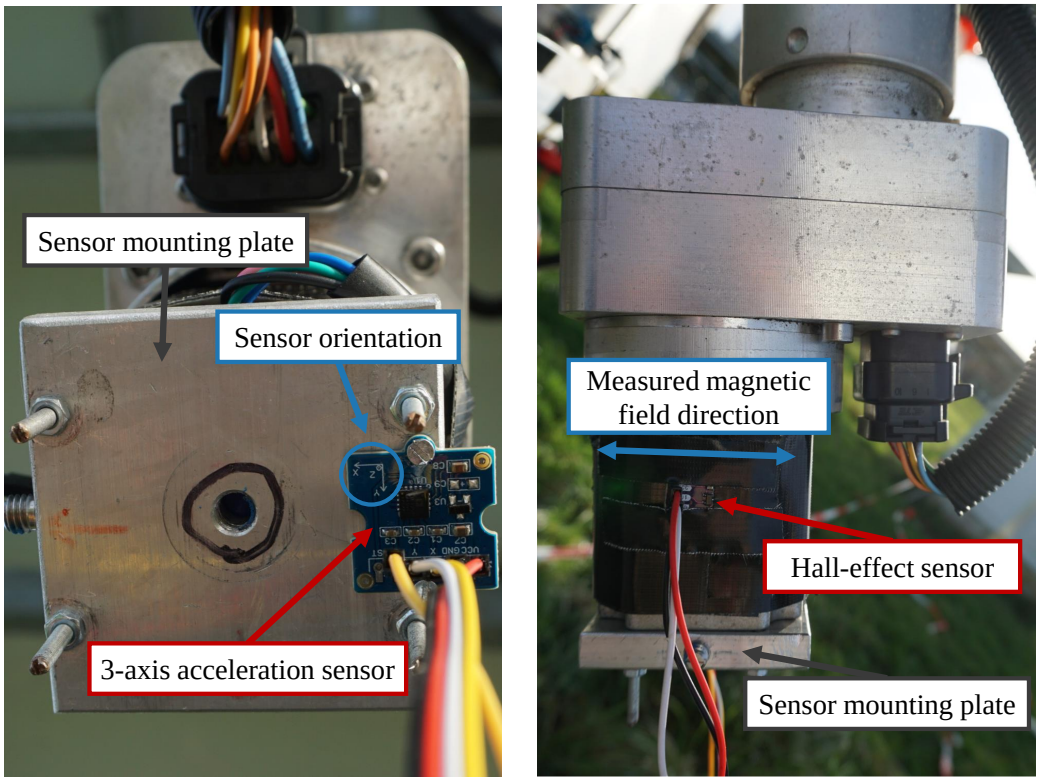
Instead of continuous long-term monitoring, the measurement campaign comprises a series of short-term experimental runs, each of which lasts from a few minutes to several hours. The measurement campaign also includes continuous 24-h field measurements investigating the stability and monitoring capability of the developed system under prolonged outdoor operation. The experiments are repeated multiple times to ensure the reproducibility of the observed signal characteristics, resulting in a total effective measurement time of approximately 330 h.

3.2.3. Implementation of the Measurement System in the Heliostat Field

For the sensor installation, first the motor housing cover has to be removed. Afterwards, a custom designed metallic sensor mounting plate with pre-drilled threaded holes is screwed into the underside of the motor. This plate enables various sensors to be indirectly mounted to the motor while ensuring a rigid, near 1:1 mechanical coupling.

The 3-axis accelerometer is mounted on this plate as shown in Figure 6a, with the orientation of its three measurement axes illustrated in Figure 7. Due to the geometrically

predefined mounting position, sensor orientation only affects the sign of the measured acceleration in the x- and y-directions. In contrast, the Hall-effect sensor is mounted laterally on the motor housing as depicted in Figure 6b. Since the motor wall is thin and the internal coils are located directly beneath it, screw fixation is not feasible. Instead, waterproof outdoor adhesive tape is tightly wrapped around the motor, and the sensor is fixed onto this layer with additional tape. Correct sensor orientation must be ensured, as the employed Hall-effect sensor captures the magnetic field along one single measurement-axis.



(**a**) (**b**)

Figure 6. Sensor installation on the motor housing of one heliostat axis: (**a**) 3-axis accelerometer mounted on the metallic sensor mounting plate. (**b**) Laterally mounted Hall-effect sensor. Sensors are highlighted in red, measurement directions and orientation information in blue, and additional annotations in dark grey.

The installation procedure has to be carried out separately for both HDUs. Once mounted, the sensors are connected to the analogue signal conditioning unit which is then connected to the Arduino (cf. Figure 4a). The wiring scheme is as follows: the sensors are powered via the Arduino 5 V supply pin and connected to ground through the GND pin. The analogue sensor signals, either directly from the sensor or after signal conditioning, are routed to the Arduino analogue input pins. To simplify wiring, a Grove shield is mounted on the Arduino, enabling straightforward connection via Grove (Seeed Studio, Shenzhen, China) extension cables. Due to the large movements of the heliostat being actively induced during the measurements, the cables must be given sufficient slack (of up to 50%). This is necessary to compensate for the resulting change in distance between sensors and the Arduino. For outdoor operation, the sensors are coated with an electronics protective lacquer to prevent moisture ingress, while keeping the electrical connectors uncovered. The Arduino microcontroller itself is placed in a weatherproof enclosure at the base of the heliostat.

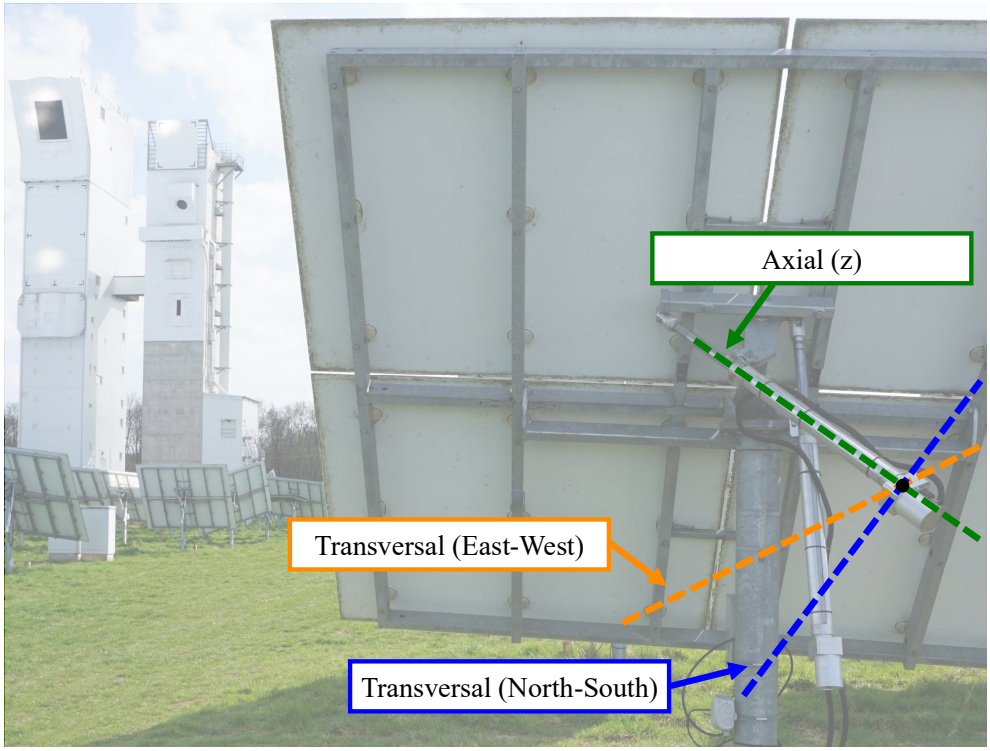


Figure 7. 3-axis accelerometer measurement axes used for the vibration measurements at the HDUs, illustrating the respective axial and transversal measurement directions. The three mutually orthogonal measurement axes are exemplarily shown for the HDU corresponding to heliostat-Axis 2. The same convention is applied to heliostat-Axis 1.

3.3. Data Analysis and Evaluation Strategy

The subsequent analysis of the recorded sensor signals X_{measured} aims to identify reproducible, condition-sensitive deviations ΔX from an expected HDU baseline behaviour X_{baseline} obtained under comparable operating conditions as for X_{measured}. In general, the deviation $\Delta X^{(i)}$ can be represented as

$$\Delta X^{(i)} \equiv \mathcal{D}\left(X^{(i)}_{\text{measured}}, X^{(i)}_{\text{baseline}}\right) \sim X^{(i)}_{\text{measured}} \text{ “}-\text{” } X^{(i)}_{\text{baseline}}, \tag{4}$$

where $\mathcal{D}(\cdot)$ denotes the respective comparison used to quantify the difference between the measured and baseline characteristics, while the superscript (i) identifies the corresponding HDU. Depending on the analysis, $\mathcal{D}(\cdot)$ may represent, for example, a visual comparison of corresponding signal traces or a comparison of characteristic minimum and/or maximum values. The symbolic “$-$” notation in Equation (4) therefore indicates a conceptual comparison with the baseline rather than a direct sample-wise subtraction of the underlying time series.

The $\Delta X^{(i)}$ may indicate emerging operational anomalies or maintenance needs for the corresponding HDU (i). Depending on the respective experiment, time-domain and/or frequency-domain signal characteristics are evaluated. In the analysis, each HDU can be compared both with its own reference behaviour at different points in time and/or with the corresponding behaviour of the other investigated heliostats (and their corresponding HDUs) under comparable operating conditions. Thus, $X^{(i)}_{\text{baseline}}$ is represented either by $X^{(i)}_{\text{baseline}} = X^{(i)}(t)|_{t=t_{\text{hist.}}}$ for a temporal, historic reference of the same HDU or by $X^{(i)}_{\text{baseline}} = X^{(j)}(t)$ with $i \neq j$ for a cross-HDU reference under comparable operating conditions. The analysis therefore focuses primarily on relative changes from expected baseline

behaviour in the recorded signals (such as changes in vibration amplitudes or dominant spectral components) rather than on individual absolute measurement values.

Potential confounding influences are considered explicitly before a deviation $\Delta X^{(i)}$ according to Equation (4) is attributed to the corresponding HDU (i):

- Temperature-related effects and long-term sensor drift are assessed using continuous 24 h stationary measurements (cf. Section 4.1.3), while
- Wind-induced effects are evaluated using simultaneously recorded ultrasonic anemometer data and corresponding temporal and correlation analyses (cf. Section 4.3.3).
- Sensor positioning effects are minimised by using the custom-designed metallic sensor mounting plate with pre-drilled threaded holes to ensure a highly reproducible sensor placement across different measurements (cf. Section 3.2.3).
- Mechanical cross-axis coupling effects through the common heliostat structure are expected to remain largely reproducible under identical movement sequences, since the controlled heliostat movement sequences (cf. Section 3.2.1) provide consistent excitation patterns for the investigated HDUs, while
- Possible electromagnetic cross-axis coupling effects are considered separately during interpretation (cf. Section 4.1.4).

Accordingly, a deviation $\Delta X^{(i)}$ is interpreted as HDU-related abnormal behaviour only if it is reproducible under comparable operating conditions and if it is consistently associated with the corresponding HDU operation or movement phase. It must also differ from the baseline behaviour observed for the same HDU over time or across HDUs. Additionally, the deviation must not be reasonably attributable to temperature, wind, sensor positioning, or known mechanical or electromagnetic cross-axis coupling effects.

4. Experimental Results and Discussion

This section is structured as follows: First, the ACMS is validated in Section 4.1, followed by a sensitivity analysis in Section 4.2. Subsequently, Section 4.3 presents an exemplary application of the ACMS, while Section 4.5 compares the costs of the ACMS with the total costs of a heliostat.

The data underlying this study are openly available via Zenodo [50], with the data repository and metadata designed to facilitate findability, accessibility, interoperability, and reusability (FAIR principles). This enables independent reproduction of the presented analyses and provides a reusable reference dataset for future benchmarking and method development in HDU condition monitoring. To the best of the authors' knowledge, the published dataset represents the first openly available collection of measurement data dedicated to sensor-based monitoring of HDUs.

4.1. Validation of the ACMS

Using the extensive set of measurements collected during the field campaign, the ACMS introduced in Section 3 is validated. It should be noted that the ACMS was developed through an iterative process involving multiple preliminary tests and successive refinements based on experimental results during the field measurement campaign.

4.1.1. Discussion of the Selected ACMS Sampling Frequency

The selected ACMS sampling frequency of $f_{\text{chosen}} = 1\,\text{kHz}$ (cf. Equation (2)) has to be considered in the context of the Nyquist–Shannon sampling theorem. Accordingly, frequency components below $f_{\text{Nyquist}} = f_{\text{chosen}}/2 = 500\,\text{Hz}$ can, in principle, be uniquely resolved, whereas higher-frequency components cannot be uniquely identified and may be mapped into the lower-frequency range by aliasing. Thus, the ACMS developed in this study does not provide comprehensive high-frequency diagnostics and it is impor-

tant to note that the ACMS cannot capture all potentially relevant HDU-related signal characteristics. For example, potentially condition-sensitive vibration components occurring predominantly in the kilohertz range would require substantially higher sampling frequencies compared to $f_{\text{chosen}} = 1\,\text{kHz}$.

However, this limitation should be evaluated against the background of the intended cost-efficient and scalable monitoring concept. As the ACMS is based on an Arduino-compatible microcontroller architecture, the maximum achievable sampling rate is inherently limited (cf. Equation (1)), especially when multiple sensor channels are acquired simultaneously. The objective of this study is not to reproduce the capabilities of a high-bandwidth industrial data acquisition system, but to investigate which condition-sensitive information can be obtained reliably with a cost-efficient monitoring system. More specifically, increasing the sampling frequency f_{chosen} would extend the accessible diagnostic bandwidth. However, this would come at the cost of higher acquisition requirements, data throughput, storage demand, and system complexity. Consequently, the suitability for large-scale heliostat field deployment would be reduced.

Overall, the chosen sampling frequency of $f_{\text{chosen}} = 1\,\text{kHz}$ (cf. Equation (2)) should not be understood as universally sufficient for detecting all possible HDU-related signal characteristics. Nevertheless, it provides an adequate temporal and spectral basis for the monitoring objectives investigated in this study, as demonstrated by the measurement results and corresponding analyses presented in the following subsections.

4.1.2. Characteristics of the Recorded Operational Data Using Analogue Signal Conditioning

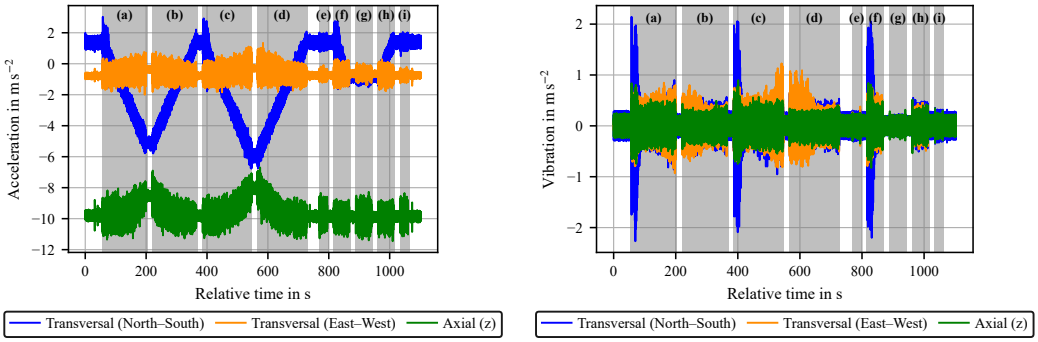
In Figure 8, the signals for Axis 1 recorded by the 3-axis acceleration sensor are shown. The sensor measures vibrations in three directions: two transversal directions (North–South and East–West) and one axial direction, which is, by definition, aligned with the actuator motion (extension/retraction). The North–South designation refers to the real-world geographical coordinate system. During the measurement, the two heliostat axes were actuated in a sequence of nine movement steps labelled from (a) to (i), including individual, simultaneous, and opposing extension and retraction movements, as documented in Figure 5.

Comparing Figure 8a (raw signal without analogue signal conditioning) and Figure 8b (signal with analogue signal conditioning), the effect of the analogue signal conditioning becomes clearly visible. The reason for the pronounced sawtooth-like behaviour of the blue curve in Figure 8a is that the 3-axis accelerometer intrinsically measures the gravitational acceleration g in addition to the dynamic vibration components. During heliostat motion, the heliostat's orientation in space changes, causing the projection of the gravitational acceleration onto the three sensor axes to vary over time. As a result, the measured acceleration signal is dominated by the slowly varying gravity component, which masks the actual vibration signatures.

The results shown in Figure 8b confirm that using the analogue signal conditioning largely removes this effect. This is primarily due to the first-order high-pass filter integrated into the analogue signal conditioning stage (cf. Section 3.1.3). Since gravitational acceleration is static and its projection onto the accelerometer axes changes only slowly during heliostat motion, the resulting low-frequency contribution is effectively attenuated by the high-pass filter. The underlying mathematical description of the high-pass filter behaviour is provided in Appendix A.1.

Moreover, as can be seen in Figure 8b, using the analogue signal conditioning stage centres the signal around the zero line, thereby yielding measurement signals that are more interpretable. Therefore, the conditioned signal is used for all subsequent analyses. During the nine movement steps visualised in Figure 8b, the vibration level is noticeably increased

compared with the time intervals in which the heliostat remains stationary, where only background noise is recorded.



(**a**) (**b**)

Figure 8. 3-axis acceleration and 3-axis vibration signals measured at Axis 1 during the nine-step movement sequence defined in Figure 5, using the measurement-axis convention illustrated in Figure 7. The shaded grey regions indicate the individual movement intervals. (**a**) Raw accelerometer signals, including the gravitational acceleration component g, which results in comparatively large acceleration amplitudes. (**b**) Corresponding signals after analogue signal conditioning, where the gravitational acceleration component g is removed such that the y-axis represents the resulting vibration signals.

Furthermore, distinct differences in the vibration patterns can be observed between the movement steps (a–i). As an illustrative example, the intervals (e,g,i) show only minor vibration increases above the background noise level. According to Figure 5, only Axis 2 is actuated during these steps, while Axis 1 remains stationary. The observed signals therefore originate solely from mechanical coupling effects between the two axes. Although the vibration patterns observed in the remaining movement steps are likewise physically explainable, their detailed interpretation is beyond the scope of this validation section. Overall, the results suggest that using an analogue signal conditioning stage is a practical and effective way of improving the quality and interpretability of the recorded sensor signals.

4.1.3. Long-Term Data Acquisition Stability Under Outdoor Operation

Reliable long-term monitoring of HDU operation requires the ACMS to maintain stable and continuous data acquisition over extended periods. Therefore, continuous 24-h-stability field measurements are conducted while the heliostat remains stationary (in its stow position) throughout the entire measurement period.

The experimental validation of the operation of all four sensor channels (cf. Section 3.1.1) over this 24-h duration (cf. Figures A1 and A2) also supports the applicability of the ACMS to shorter multi-hour measurements. In particular, the very high data availability of 99.92% demonstrates robust continuous data acquisition. Moreover, as listed in Table A1, the three vibration channels contain only small fractions of samples outside the interval-specific statistical ranges and also exhibit comparatively low temporal sensor drift. For reference, a normally distributed signal would statistically contain approximately 4.55% and 0.27% of its samples outside the $\mu \pm 2\sigma$ and $\mu \pm 3\sigma$ ranges, respectively. For the three vibration channels, the corresponding $\mu \pm 2\sigma$ exceedance fractions range from 0.416% to 3.480% and are therefore below the Gaussian reference value. For the $\mu \pm 3\sigma$ range, only 0.00003% to 0.02073% of the samples are outside the respective bounds. Together with the comparatively low σ-normalised drift rates of 2.57% h^{-1}, 7.61% h^{-1}, and 4.09% h^{-1}, these results indicate a high stability of the vibration signals and support their suitability for extended long-term monitoring.

In contrast, the Hall-effect sensor shows a higher fraction of samples outside the statistical reference ranges. The respective exceedance fractions amount to 4.884% and 0.572% for the $\mu \pm 2\sigma$ and $\mu \pm 3\sigma$ ranges as listed in Table A1. In particular, the exceedance fraction beyond 3σ is higher than the corresponding Gaussian reference values. In addition, the Hall-effect sensor exhibits a distinctly larger σ-normalised temporal drift compared to the vibration sensors, at approximately one quarter of the average interval standard deviation per hour, namely 26.18% h^{-1} (cf. Figure A2). This behaviour could be the result of diurnally varying temperature conditions in the outdoor environment influencing the sensor response. This potential correlation was therefore taken into account in subsequent analyses. It should be noted that the investigated $\mu \pm n\sigma$ ranges (for $n \in \mathbb{N}$) are used here exclusively to characterise signal stability under stationary conditions and do not represent fixed anomaly detection thresholds.

4.1.4. Comparison with Conventional Industrial-Grade Sensors

A qualitative comparison between the industrial-grade reference sensors and the ACMS is presented in Figure 9. In Figure 9a approximately 1.5 s of data during the start-up phase of the heliostat motor are shown. The motor start-up begins around $t \approx 0.2$ s, characterised by a damped transient response, with decreasing current amplitudes and a simultaneous increase in signal frequency over time. This qualitative comparison reveals a strong correspondence between the measured current and the magnetic flux density. Notably, there is a distinct double-peak structure in the magnetic field that aligns with the peaks of the two phase currents. This strong correspondence is particularly evident in the zoomed view in Figure 9b, where the closely overlapping signal trajectories demonstrate that the different sensor types capture the same temporal oscillation behaviour. Therefore, the low-cost Hall-effect sensor is capable of capturing a signal closely related to the behaviour of the motor current.

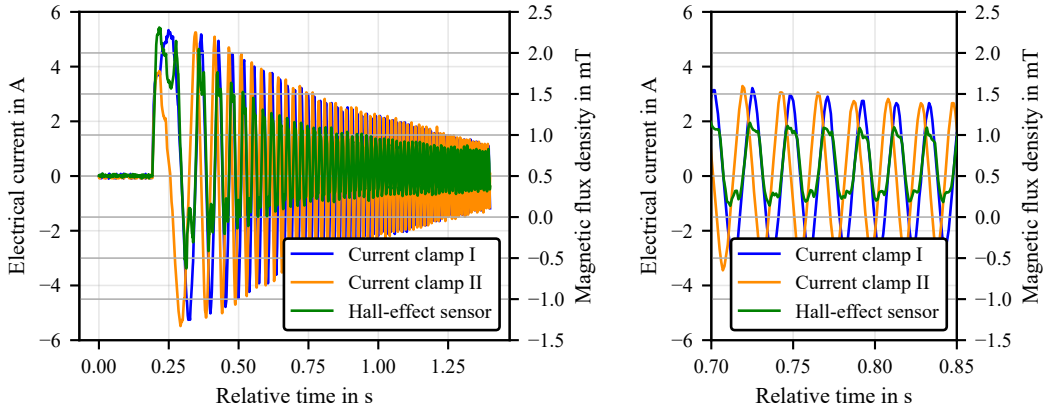


Figure 9. Comparison of the motor phase currents measured with two current clamps and the magnetic flux density measured with a Hall-effect sensor during the start-up phase of the heliostat motor of Axis 1. Current Clamp I (i.e., $I_1(t)$) and Current Clamp II (i.e., $I_2(t)$) are attached to the two motor phase conductors, while the Hall-effect sensor (i.e., $B(t)$) measures the overall resulting magnetic flux density generated by both phase currents: (**a**) Full time-domain representation; (**b**) Detailed view between 0.70 s and 0.85 s.

Besides the qualitative comparison described above, an additional semi-quantitative assessment is performed: The underlying assumption is that, to first order, the magnetic flux density measured at the Hall-sensor position $B(t)$ can be represented as a linear superposition $B_{\text{fitted}}(t)$ of the magnetic field contributions associated with the two motor-phase currents $I_1(t)$ and $I_2(t)$ as

$$B_{\text{fitted}}(t) = \beta_0 + \beta_1 I_1(t) + \beta_2 I_2(t), \tag{5}$$

where β_0 represents the constant offset term and β_1 and β_2 describe the linear contributions of the individual phase currents. Accordingly, the purpose of this semi-quantitative analysis is to assess how well $B(t)$ can be represented by $B_{\text{fitted}}(t)$ from the simultaneously measured phase currents. For this purpose, the two current clamp signals are linearly interpolated onto the timestamps of the Hall-effect sensor measurement, such that $B(t)$, $I_1(t)$, and $I_2(t)$ refer to the same instants in time.

The regression coefficients in Equation (5) are determined by least squares fitting, and the resulting model prediction $B_{\text{fitted}}(t)$ is subsequently evaluated using the coefficient of determination R^2 and the root mean squared error (RMSE) as presented in Figure 10. The time-domain representation (cf. Figure 10a) illustrates how closely the fitted signal follows the measured magnetic flux density during motor start-up, while the corresponding scatter representation (cf. Figure 10b) provides an additional point-wise comparison between $B(t)$ and $B_{\text{fitted}}(t)$. It should be noted that the reported R^2 and RMSE characterise the in-sample fit quality, since the regression coefficients are determined from the same data used for evaluating the model.

Nevertheless, the resulting value of $R^2 = 0.850$ indicates a strong correspondence in the temporal signal behaviour captured by the industrial-grade current measurements and the Hall-effect sensor measurement. At the same time, the remaining structure observed in the residuals indicates that the first-order linear model $B_{\text{fitted}}(t)$ does not fully reproduce all details of $B(t)$, particularly during the transient start-up behaviour. Therefore, the model should be considered as a simplified approximation of the relationship between the phase currents and the measured magnetic field.

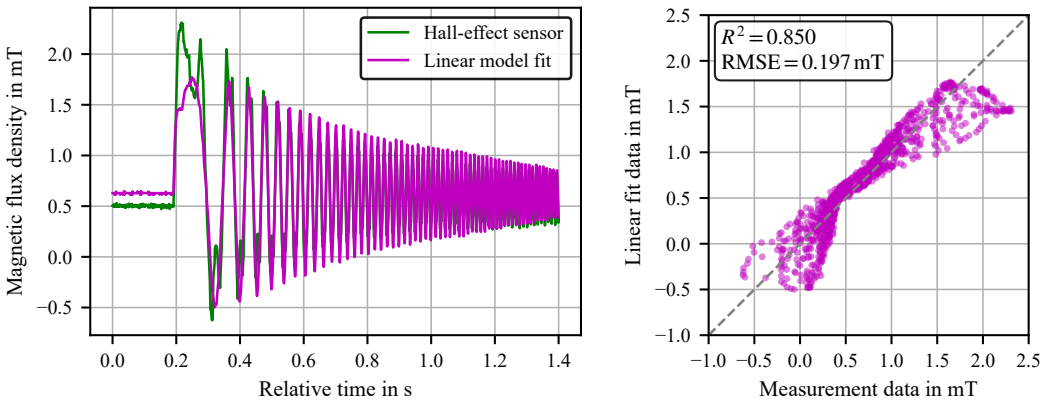


Figure 10. Quantitative comparison between the measured Hall-effect sensor data and the corresponding current clamp data. The linear model in Equation (5) is fitted to the current data (i.e., $I_1(t)$ and $I_2(t)$) measured during the start-up phase of the Axis 1 heliostat motor: (**a**) Time-domain comparison between the measured magnetic flux density $B(t)$ and the corresponding model prediction $B_{\text{fitted}}(t)$; (**b**) Modelled values plotted against the measured Hall-effect sensor data, with the dashed diagonal line indicating ideal agreement. The coefficient of determination R^2 and the root mean squared error (RMSE) quantify the in-sample fit quality.

More generally, the objective of the ACMS is not to reproduce the industrial-grade reference measurements in terms of their absolute values. Rather, the relevant requirement for the intended condition monitoring application is that changes in the underlying operational behaviour are reflected consistently in the low-cost sensor data. For example, a change in the amplitude or temporal characteristics of the motor-phase currents should result in a corresponding change in the magnetic flux density measured by the Hall-effect sensor.

In this context, the current clamp measurements and Hall-effect sensor measurements are considered to be complementary representations of the motor behaviour rather than being directly interchangeable measurements of the same physical quantity. Therefore, the semi-quantitative comparison in Figure 10 complements the qualitative validation presented in Figure 9 by demonstrating the extent to which the temporal information contained in the industrial-grade current measurements is also reflected in the Hall-effect sensor signal.

One limitation of the Hall-effect sensor becomes apparent when the magnetic fields from both heliostat axes are superimposed. During a particular test measurement, for example, the orientation of the heliostat temporarily brought the motors of both axes into close proximity, resulting in a non-negligible superposition of their magnetic fields. While such effects can be identified and corrected during the subsequent data analysis, current clamps are inherently less susceptible to this interference because they measure the current directly at the conductor. Nevertheless, the Hall-effect sensor offers a significant practical advantage in addition to its lower cost: It can be installed externally without requiring direct access to the current-carrying wires, thereby substantially simplifying sensor installation under outdoor field conditions.

4.2. Sensitivity Analysis of the ACMS

To assess the sensitivity of the ACMS introduced in Section 3, a controlled experiment was conducted in which characteristic signal signatures were deliberately induced in the measurement data. This served as an example of system-level validation.

4.2.1. Concept of the Experimental Study with Controlled Motor Phase Resistance Variation

The underlying idea of this experiment is to intentionally modify the electrical operating conditions of the motor in order to induce measurable changes in the magnetic flux density, which may also lead to observable variations in the vibration behaviour.

The motor system comprises two coil pairs connected to a controller unit. During the experiment, an external resistor R is inserted in series with one coil pair, while the other coil pair remains directly connected to the controller. Varying the value of R adjusts the electrical load of the affected phase, thereby altering the current distribution within the motor windings. Consequently, changes in the resulting magnetic flux density inside the motor are expected, which can be detected by the Hall-effect sensor.

The resistance configuration sequence

$$\boldsymbol{R} = \left\{ \underbrace{0.0,\ 0.0,\ 0.1,\ 0.2,\ 0.3,\ 0.3,\ 0.5}_{0\,\Omega \text{ to } 1\,\Omega \text{ interval}}, \underbrace{1.0,\ 1.1,\ 1.2,\ 1.3,\ 1.5}_{1\,\Omega \text{ to } 2\,\Omega \text{ interval}}, \underbrace{2.0,\ 2.1}_{2\,\Omega \text{ to } 3\,\Omega}, \ldots, \underbrace{6.0,\ 6.1}_{6\,\Omega \text{ to } 7\,\Omega}, 0.0 \right\} \Omega \quad (6)$$

varies R systematically between $R_{\text{min}} = 0.0\,\Omega$ and $R_{\text{max}} = 6.1\,\Omega$ using a combined stepping strategy: Around selected operating points, closely spaced resistance pairs with increments of $0.1\,\Omega$ were examined to resolve small changes in the system response. The overall range is extended in approximately $1\,\Omega$ intervals to cover a broader parameter space. Additionally, reference measurements with no additional series resistance (i.e., $R = 0\,\Omega$) are conducted before and after the experiment. This provides a baseline for scientific control and verifies measurement stability.

The same heliostat movement sequence consisting of an extension and subsequent retraction of the actuator of Axis 1 by 20,000 motor steps is executed for each resistance value $R \in \boldsymbol{R}$ (cf. Equation (6)). It should be noted that all experiments were performed on Axis 1 only since both axes are electrically identical. For this reason, analysing a single axis is considered sufficient. It should be noted that the analogue signal conditioning stage (cf. Appendix A.1) is not used for the experiments discussed in this Section 4.2.

4.2.2. Magnetic Flux Density Analysis

The resulting measurement data obtained from the Hall-effect sensor are presented in Figure 11. The signal consists of a sequence of characteristic patterns corresponding to the repeated actuator movements as discussed above. Each pattern exhibits distinct peaks of up to approximately 1.5 mT in amplitude during the motor start-up and braking phases. Between these phases, there is a quasi-stationary phase (i.e., during steady motor operation) exhibiting an amplitude of approximately 0.5 mT.

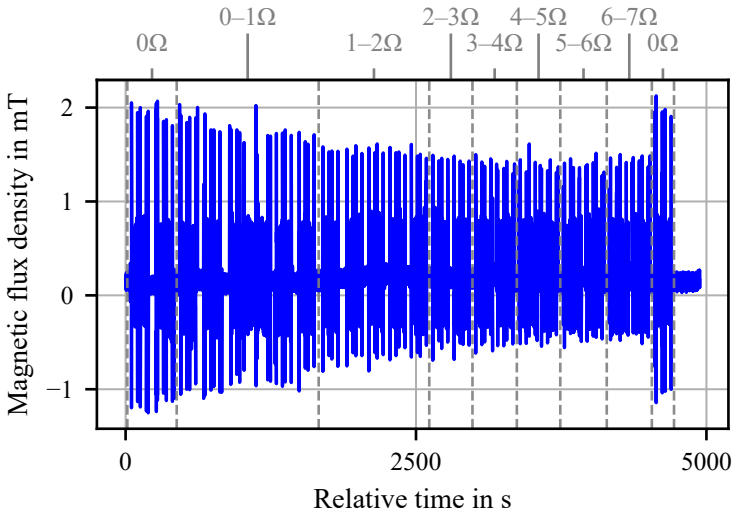


Figure 11. Measured magnetic flux density of Axis 1 in transversal (North-South) direction. The vertical grey dashed lines indicate the resistance intervals corresponding to the resistance configuration sequence given by Equation (6).

Since the resistance configuration sequence in Equation (6) increases monotonically (except for the final reference measurement), a reduction in the current through the affected phase is expected based on basic circuit considerations (Ohm's law: $I = U/R$). Apart from minor fluctuations, this leads to the observed overall trend of a reduction in magnetic flux density amplitude from left to right in the plot in Figure 11, which is consistent with the physical expectation. For instance, for $R \gtrsim 3\,\Omega$, the magnetic field amplitude is reduced by approximately one third compared to the initial state. At the end of the experiment, the reference measurement with $R = 0\,\Omega$ confirms that the HDU returns to its initial operating state, with the magnetic flux density amplitude returning to its initial level.

Furthermore, Figure 11 demonstrates that even slight variations in the electrical properties of the drive system (represented here by changes in the motor phase resistance) result in clearly detectable changes in the measured magnetic field signatures. A supplementary trend-based amplitude analysis further suggests that individual increments in the order of $R \approx 0.1\,\Omega$ cannot be reliably resolved. However, changes of the order of $R = 1\,\Omega$ can be identified with high confidence. In a maintenance context, this sensitivity of the ACMS is highly valuable, since threshold-based comparisons of the signal characteristics can support the early identification of emerging abnormal electrical operating behaviour.

4.2.3. Vibration Analysis

While conducting the experiments presented in this Section 4.2, it was observed that, for $R \gtrsim 3\,\Omega$, the actuator of Axis 1 exhibits a noticeably louder operating noise. This observation motivates an additional inspection of the vibration signals.

As shown in Figure 12, the fast Fourier transform (FFT) spectrum of the vibration signal measured at Axis 1 reveals clear changes in the frequency-domain as R increases. For clarity, only three representative resistance configurations (cf. Equation (6)) are shown. In particular,

for the interval 6–7 Ω (green curve), several vibration peaks are significantly higher than in the $R = 0\,\Omega$ baseline condition (blue curve). In parts of the higher-frequency range around 400 Hz, amplitude increases by a factor of approximately 2–4 can be observed. These results suggest that the proposed measurement setup is sensitive not only to variations in the magnetic flux density, but also sensitive to vibration changes induced by altered electrical operating conditions of the motor.

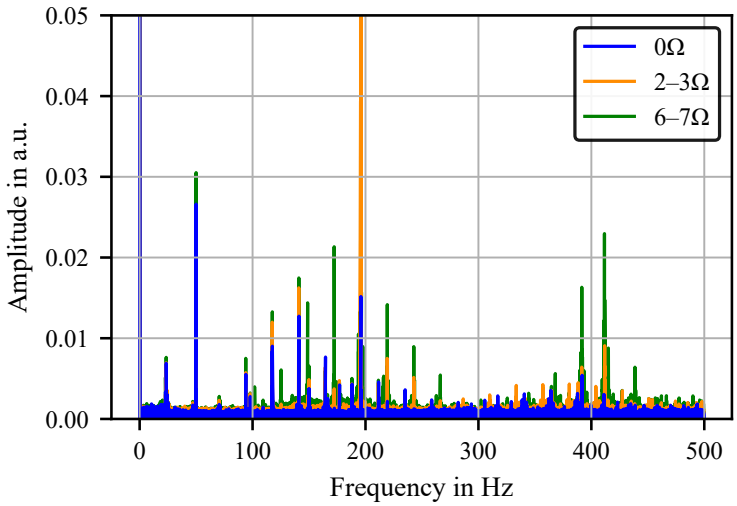


Figure 12. Fast Fourier transform (FFT) spectra of the measured vibration signals of Axis 1 in transversal (East-West) direction. The plotted data refer to the vibration in transversal (East-West) direction. The three curves correspond to representative regions of the resistance configuration sequence defined in Equation (6).

As already discussed, Figure 11 indicates that the R-induced decrease in the magnetic flux density B is consistent with Ohm's law, since $R \uparrow \Rightarrow I \downarrow \Rightarrow B \downarrow$. In addition to this first effect, R also modifies the relative phase relationship $\Delta\varphi$ between the motor-phase currents, i.e., $R \uparrow \Rightarrow \Delta\varphi \updownarrow$, as a second effect. Such R-dependent changes $\Delta\varphi_{\text{initial}} \rightarrow \Delta\varphi_{\text{modified}}$ can result in a non-uniform rotation of the magnetic field, whose interaction with the rotor generates the electromagnetic torque required for motor motion. Consequently, this leads to increased torque ripple and vibration excitation as can be seen in Figure 12 (Section Electrical Interpretation of the Series-Resistance Experiment for more details).

Although the resistance range around 6 Ω to 7 Ω shown in Figure 12 represents an intentionally exaggerated loading condition that is unlikely to occur during normal operation, similar amplitude increases are already observable at lower resistance values. In particular, a weaker increase is visible in the intermediate range around 2 Ω to 3 Ω (orange curve). This suggests that even moderate electrical deviations can produce detectable changes in the vibration signals.

4.3. Exemplary Demonstration of the ACMS

Prior to the measurement campaign, all eight of the monitored heliostats have been operating under regular plant conditions, and no abnormalities have been reported by the operating personnel. Accordingly, consistent behaviour with typical, characteristic signal patterns is expected across the monitored heliostats. However, the measurement data for heliostat 12023 exhibit clear deviations from these patterns, indicating anomalous behaviour.

For this reason, the 12023-heliostat was selected for detailed analysis: All data presented in this subsection have been recorded during a four-hour (i.e., $T = 14{,}400$ s) measurement period. During this time, the heliostat was operated using a cyclic movement

pattern consisting of repeated execution of the first four steps of the nine-step movement sequence defined in Figure 5:

$$(a) \rightarrow (b) \rightarrow (c) \rightarrow (d) \rightarrow (a) \rightarrow (b) \rightarrow (c) \rightarrow (d) \rightarrow \ldots . \quad (7)$$

By selecting this particular movement pattern, both heliostat axes were actuated simultaneously and repeatedly extended and retracted throughout the full measurement period T, thereby providing a prolonged cyclic loading test of the HDUs.

4.3.1. Vibration Analysis

Figure 13 presents the measured vibration signals in transversal (North-South) direction for Axis 1 and Axis 2, respectively. (The North-South designation is the same as used in Section 4.1). In addition, Figure 14 illustrates the corresponding short-time Fourier transform (STFT) of the transversal (North-South) vibration signal for Axis 2.

As can clearly be seen in Figure 13a, the vibration signal initially stabilises at an almost constant amplitude of approximately $0.4\,\mathrm{m\,s^{-2}}$. However, from $t \gtrsim 7000\,\mathrm{s}$ onwards, the signal exhibits increasingly pronounced outliers. These anomalous peaks reach amplitudes exceeding $1\,\mathrm{m\,s^{-2}}$ which are therefore markedly more pronounced than the previously observed signal fluctuations. Under nominal operating conditions, the vibration level is expected to remain approximately constant, as initially observed. This expected behaviour is consistently observed across the other seven monitored heliostats.

Comparing the data measured at Axis 1 (cf. Figure 13a) with the data measured at Axis 2 (cf. Figure 13b) reveals similar temporal patterns for the two axes. In both signals, pronounced outlier peaks emerge from approximately $t \gtrsim 7000\,\mathrm{s}$ onwards. For Axis 2, however, these anomalous peaks are considerably more pronounced than those for Axis 1, reaching amplitudes of nearly $6\,\mathrm{m\,s^{-2}}$. This corresponds to approximately ten times the nominal vibration level observed during the initial phase of the measurement. Therefore, Axis 2 is considered the primary source of the observed vibration anomaly. The weaker vibration response detected on Axis 1 (cf. Figure 13a) is likely attributable to mechanical coupling between the two axes. This indicates that the underlying operational issue originates from the Axis 2 HDU.

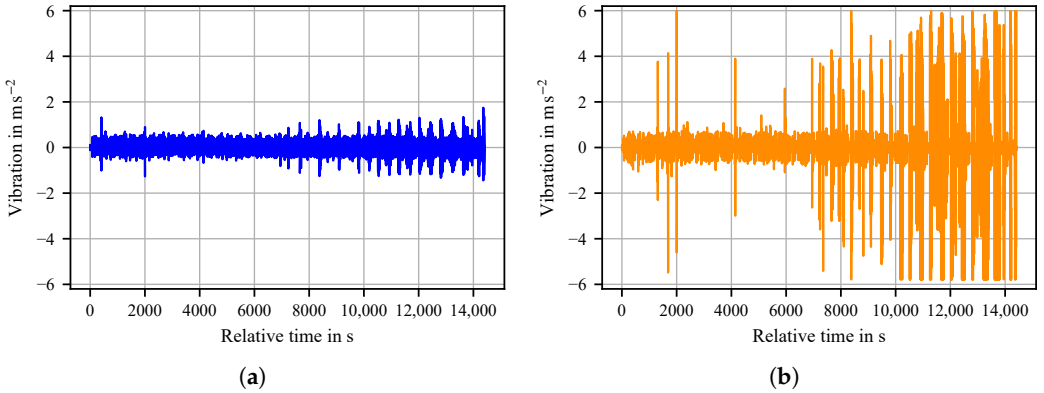


Figure 13. Measured vibration signals in transversal (North-South) direction obtained using analogue signal conditioning: (**a**) Axis 1; (**b**) Axis 2.

It should be noted that the true peak amplitudes for Axis 2 are likely higher than those shown in Figure 13b. The reason is that the vibration sensor signal reaches the measurement limit of the ACMS, which is constrained by the admissible input range $U_{\mathrm{ADC,range}}$ of the

ADC (cf. Section 3.1, Appendices A.1 and A.2). $U_{\mathrm{ADC,range}}$ and the equivalent acceleration measurement range $a_{\mathrm{ADC,range}}$ are given by

$$U_{\mathrm{ADC,range}} = [U_{\mathrm{ADC,min}}, U_{\mathrm{ADC,max}}] = [0\,\mathrm{V}, 3.3\,\mathrm{V}], \tag{8}$$

$$\Rightarrow a_{\mathrm{ADC,range}} = [a_{\mathrm{ADC,min}}, a_{\mathrm{ADC,max}}] = \left[-5.78\,\mathrm{m\,s^{-2}}, 5.99\,\mathrm{m\,s^{-2}}\right]. \tag{9}$$

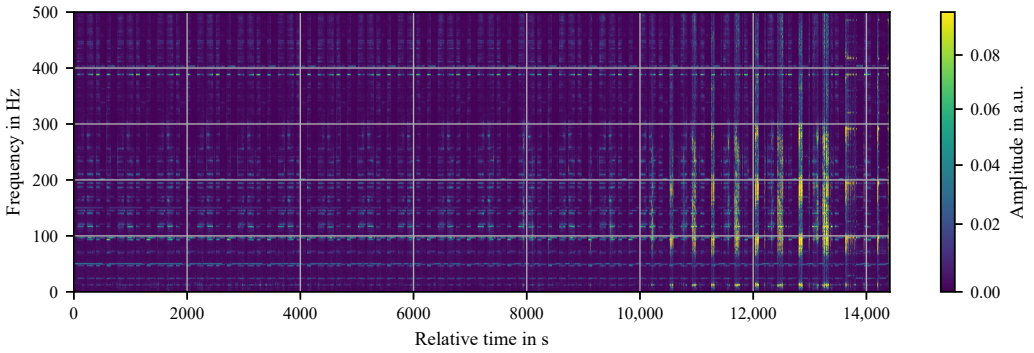


Figure 14. Short-time Fourier transform (STFT) of the vibration signal of Axis 2 in transversal (North-South) direction (cf. Figure 13b).

Input voltages outside this range (cf. Equation (8)) cannot be resolved by the ADC as distinct values. Instead, the ADC output saturates $U_{\mathrm{ADC,min}}$ or $U_{\mathrm{ADC,max}}$ respectively. With the particularly high vibration peak amplitudes occurring at Axis 2, this limit is reached. This causes the corresponding measured peak values to be clipped, preventing the exact minimum/maximum amplitudes from being resolved. Nevertheless, the presence of these high-amplitude events, their position within the respective motor movement sequence, their duration, and their pronounced amplitude relative to the baseline behaviour remain clearly identifiable. The ADC saturation therefore primarily affects the quantitative determination of the absolute peak magnitude. For the analyses presented here, however, the ADC saturation does not prevent the identification of the strongly increased and abnormal Axis 2 vibration behaviour, since the relevant temporal occurrence and characteristic signal pattern remain preserved.

The behaviour characterised by the emergence of pronounced peaks from $t \gtrsim 7000\,\mathrm{s}$ onwards can also be observed in the time-frequency representation shown in Figure 14. The STFT reveals increasingly strong anomalous events in the frequency-domain, particularly from approximately $t \approx 10{,}000\,\mathrm{s}$ onwards. These events appear as distinct, high-intensity vertical structures (yellow bands) in the spectrogram. These vertical structures indicate short-duration impulsive events with energy distributed across a broad frequency range. Such broadband characteristics are typical of transient mechanical disturbances rather than steady-state vibration components.

For both axes, in addition to the transversal (North–South) vibration components shown in Figures 13 and 14, respectively, a similar temporal trend in each case is also present in the other two measured vibration directions, albeit with a weaker amplitude.

4.3.2. Magnetic Flux Density Analysis

The analysis of the magnetic flux density focuses on Axis 2, since the previous vibration analysis identifies Axis 2 as the primary source of the observed anomalies. Unlike the vibration signals, the effects emerging for $t \gtrsim 7000\,\mathrm{s}$ are less pronounced in the magnetic flux density signals. Rather than providing global overview of the entire measurement period, as shown for the vibration data in Figure 13, a comparative perspective between the early and late stages of the measurement period is better suited. This comparison is shown in Figure 15, where the magnetic flux density recorded near the start of the measurement at

approximately $t \approx 500\,\mathrm{s}$ (blue curve) is compared with the signal recorded at $t \approx 12{,}000\,\mathrm{s}$ (orange curve).

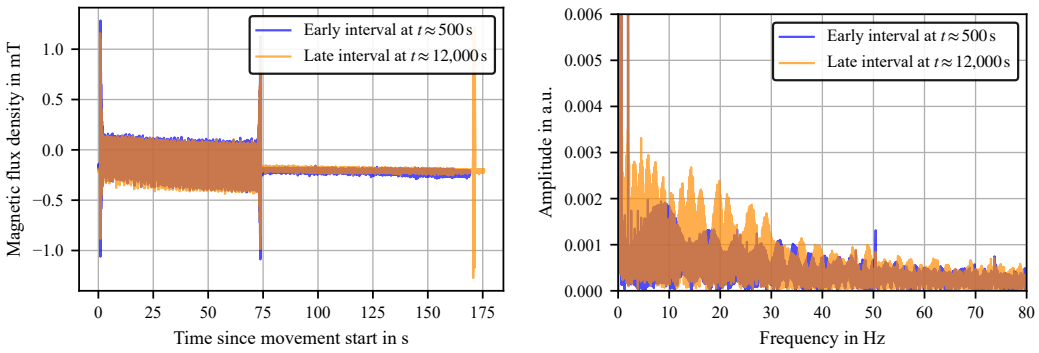


Figure 15. Comparison of early-stage and late-stage Axis 2 Hall-effect sensor measurements in transversal (North-South) direction obtained using analogue signal conditioning: (**a**) Time-domain comparison; it should be noted that the x-axis shows the time since the respective movement start, i.e., the measurements were recorded at different points in time, but both segments are aligned to start at $t = 0\,\mathrm{s}$. (**b**) Corresponding FFT-based comparison.

In the left half of the time series plot in Figure 15a (i.e., 0 s to 75 s after the start of the respective movement), two pronounced peaks can be observed in the magnetic flux density in both the early and late stages. These two peaks correspond to the motor start-up and braking phases (cf. Figure 9a). Between these two peaks, the signal exhibits a quasi-stationary phase associated with steady motor operation. In this time-domain representation, both curves (blue and orange) appear largely similar.

However, in the right half of the time series plot in Figure 15a (i.e., 75 s to 175 s after respective movement start), it can be observed that an additional motor correction movement occurs at the later stage, which is visible as the prominent orange peak at $t \approx 170\,\mathrm{s}$. This indicates that when the vibration levels become elevated (cf. Figures 13 and 14), the HDU performs extra automatic correction movements because the target position cannot be reached with sufficient accuracy. Consequently, such peaks in the magnetic flux density signal can also be interpreted as an indicator of an operational problem with the HDU.

A comparative frequency-domain analysis is performed with the corresponding FFT results shown in Figure 15a. In contrast to the time-domain representation in Figure 15b, clear differences between the blue and the orange curve become visible in the frequency-domain in the low-frequency range ($0\,\mathrm{Hz} < f < 80\,\mathrm{Hz}$). In this frequency range, the late stage data (orange curve) exhibit noticeably higher amplitudes and a larger number of discrete spectral peaks compared with the early stage data (blue curve). Moreover, the same behaviour is observed when analysing additional time segments beyond the representative comparison ($t \approx 500\,\mathrm{s}$ and $t \approx 12{,}000\,\mathrm{s}$) considered here. These observations, in agreement with the earlier presented vibration results, indicate that spectral changes emerge distinctly for $t \gtrsim 7000\,\mathrm{s}$, suggesting the onset of a pronounced change in operational behaviour rather than a slowly evolving, continuously increasing trend.

4.3.3. Evaluation of External Influences on the Measurements

In general, wind constitutes a significant external excitation source affecting heliostat behaviour, as discussed in previous studies [3,24,51]. To ensure that the observed signal patterns in the measurement data (cf. Figures 13–15) originate from operational problems of the HDU rather than from wind-induced structural vibrations, three filtering and verification steps have been applied during the analysis:

- First, measurement days are excluded from further evaluation if wind speeds of $v_{\text{wind}} = 12\,\text{m}\,\text{s}^{-1}$ or higher are recorded. (v_{wind} is calculated from the three measured wind-velocity components u, v, w as $v_{\text{wind}} = \sqrt{u^2 + v^2 + w^2}$.) This speed threshold is intentionally chosen as a conservative upper screening criterion. A wind speed of $v_{\text{wind}} = 12\,\text{m}\,\text{s}^{-1}$ corresponds to approximately Beaufort force 6 (strong breeze) and reflects wind conditions under which the STJ facility is generally not operated for safety reasons. Therefore, such measurement periods are excluded a priori. It should be noted that the Beaufort scale is used here only as an approximate reference. This is because the Beaufort scale is conventionally defined for wind measurements taken 10 m above ground level, whereas the wind sensor used for this study is installed 2.7 m above ground level—slightly above the mirror-facet height in the stow position.
- Second, the prevailing wind conditions are characterised quantitatively in detail. For the measurement period considered here (cf. Figures 13–15), the mean wind speed magnitude is $3.38\,\text{m}\,\text{s}^{-1}$, while the 95th and 99th percentiles are $5.85\,\text{m}\,\text{s}^{-1}$ and $7.06\,\text{m}\,\text{s}^{-1}$, respectively. Wind speeds exceed $5.4\,\text{m}\,\text{s}^{-1}$ (Beaufort force 4) in 8.350% of the recorded samples, while only 0.238% and 0.001% of the samples exceed $7.9\,\text{m}\,\text{s}^{-1}$ and $10.7\,\text{m}\,\text{s}^{-1}$ (Beaufort forces 5 and 6), respectively. In addition, a linear fit to the one-minute mean wind speeds yields a slope of $-0.02\,\text{m}\,\text{s}^{-1}\,\text{h}^{-1}$, indicating no systematic increase in wind speed over the measurement period. This is particularly relevant given the pronounced changes in the HDU signals shown in Figures 13–15, which occur for $t \gtrsim 7000\,\text{s}$, i.e., towards the second half of the considered measurement period. The corresponding wind speed data are shown in the lower panel of Figure 16 with the orange curve representing the full-resolution data (measurement frequency $f = 20\,\text{Hz}$) and the green curve representing the wind speed averaged over 10 s intervals. Overall, the observations suggest that the measurement period under consideration is characterised primarily by low to moderate wind speeds, with higher wind speeds occurring only as short-duration events rather than as sustained conditions.
- Third, the temporal comparison of the recorded vibration signals and prevailing wind conditions in Figure 13b reveals no apparent temporal correlation. Notably, the pronounced vibration peaks occurring for $t \gtrsim 7000\,\text{s}$ do not coincide with corresponding increases or peaks in the recorded wind speed. To further quantify whether the observed variations in the vibration level are correlated with the prevailing wind conditions, the mean wind speed and the vibration RMS are evaluated over identical 10 s intervals and compared. As can be seen in Figure 17 and as indicated by the calculated Pearson correlation coefficient of $r = -0.018 \approx 0$, there is no apparent linear relationship between the mean wind speed and the vibration level during the considered measurement period.

Therefore, the identified effects and patterns in the HDU vibration data (cf. Figure 13b) can be assumed to be largely independent of wind-induced excitation.

Moreover, no significant change in ambient temperature is observed during the relevant time period. Also, for the 12023-heliostat, no visually noticeable wind-induced deformation of the heliostat facets or other structural components is observed during the considered time period. Additionally, there are no reported disturbances of the overall heliostat field on the day of the measurement that could explain the localised response of the 12023-heliostat. Similarly, no supply voltage or grid fluctuations that could have affected the operation of the heliostat field are known to have occurred during the investigated time period. Other external factors which may influence the operation of the overall solar tower plant are also considered, such as cloud passages and the resulting short-term spatial variation or reduction in the irradiance focused onto the receiver. However, such effects cannot explain the observed signal patterns in the measurement data for a single, isolated heliostat.

Overall, these observations support the interpretation that the identified effects and patterns are not primarily caused by wind or other external factors. Instead, they appear to originate from the HDU and to reflect abnormal operational behaviour.

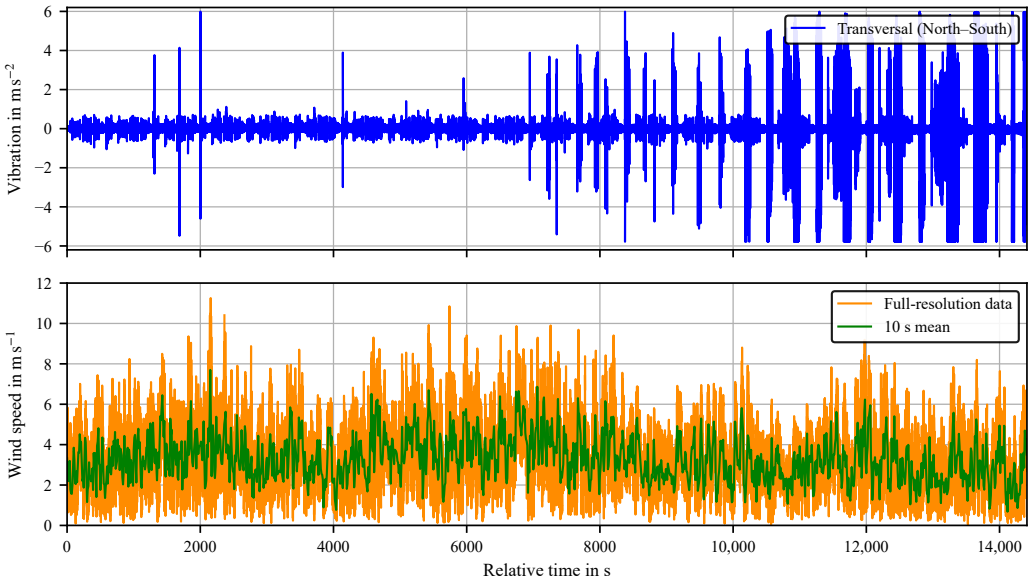


Figure 16. Temporal comparison of the vibration measurements at Axis 2 obtained using analogue signal conditioning (cf. Figure 13b) and corresponding wind conditions. In the lower panel, the full-resolution wind speed data with $f = 20$ Hz (orange curve) are shown together with the corresponding 10 s mean values (green curve).

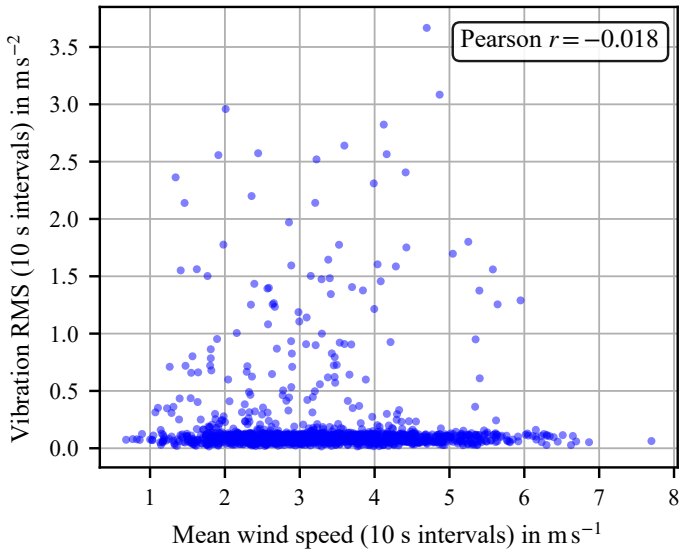


Figure 17. Correlation analysis between measured wind speed and vibration measurements at Axis 2 obtained using analogue signal conditioning (cf. Figure 13b). The comparison and Pearson correlation coefficient r are calculated over identical 10 s intervals, with each scatter point representing one of these intervals.

4.3.4. Operational Implications for Condition-Based Maintenance

Although the 12023-heliostat remained operational throughout the entire measurement period of $T = 14{,}400$ s (=4.0 h) and continued to execute the commanded movements (cf. Equation (7)), the observed anomalies suggest that a complete operational failure may occur in the near future. However, no dedicated physical inspection or disassembly of the HDU of 12023-heliostat is documented which could have been used to determine the

underlying root cause. When considering the potential effects of ageing, it should be noted that the HDUs investigated in this study (cf. Equation (3)) were installed as part of the field retrofit, which began in 2020 and lasted approximately three years [49]. Therefore, the HDUs have been in service for approximately 3–6 years at the time of the measurements presented in Figure 13. However, the exact histories of HDU installation and replacement, as well as complete records of accumulated operating cycles, are not available. As the STJ is mainly operated as a research facility rather than under continuous commercial operating conditions, the accumulated operational exposure is expected to be substantially lower than that associated with continuous daily operation. Accordingly, the condition monitoring results are primarily interpreted by comparing the investigated heliostats (cf. Equation (3)), which are expected to have accumulated broadly similar operating times and to have experienced comparable environmental conditions. Therefore, any deviations observed in the measurement data for an individual HDU should be assessed in relation to the behaviour of the HDUs of the other heliostats in the same group, rather than against an absolute, lifetime-based reference point.

Within the proposed ACMS, changes in the HDU measurement data could provide an early indication of emerging abnormal behaviour. Even a simple, low-level monitoring strategy based on detecting abnormal vibration behaviour using thresholds would likely be sufficient to identify the affected heliostats. For example, the operational problems identified for the Axis 2 HDU of the 12023-heliostat could potentially be detected before an unexpected failure occurs. Thus, the identified deviations would provide an early indication of an emerging problem, enabling O&M personnel to initiate targeted inspections, root-cause analyses and specific maintenance actions. No comparable operational problems are observed for the other heliostats (cf. Equation (3)) investigated during the measurement campaign.

4.4. Transferability of the Results from the Investigated Heliostat Group to Large-Scale Heliostat Fields

The measurement campaign presented in this study investigates a group of eight neighbouring heliostats (cf. Equation (3)) selected without prior screening with respect to the experimental objectives. This number corresponds to approximately 0.4% of the more than 2000 heliostats installed at the STJ [49]. Consequently, this group cannot be considered statistically representative of the entire heliostat field.

On the one hand, specific quantitative signal amplitudes, specific spectral characteristics, quantitative thresholds, and anomalies identified in individual HDUs cannot be extrapolated directly to the entire heliostat field (i.e., to all HDUs). Similarly, this study does not systematically investigate the influence of different heliostat locations within the field on the measured HDU behaviour. For instance, heliostats positioned near the outer boundaries oof the field may experience different local wind conditions than heliostats located further within the field, as documented in [52]. However, using neighbouring heliostats can also be advantageous for the comparative analyses conducted in this study. This is because the corresponding HDUs are expected to have experienced broadly similar environmental conditions and operating histories, which facilitates the identification of relative HDU-related differences.

On the other hand, the main outcomes that can be transferred from this study are the developed methodology and the ACMS concept. This includes the sensor selection and data logging architecture, the controlled heliostat movement sequences, as well as the baseline-based comparison strategy for the subsequent evaluation, as explained in detail in Section 3. Furthermore, fundamental operational signal characteristics from the baseline HDU operation, such as characteristic motor start-up and braking patterns, are also expected to be transferable.

Overall, the objective of this study is the development and experimental field validation of the proposed ACMS, rather than to conduct a comprehensive condition assessment of an entire heliostat field. In this context, the results presented here provide strong evidence of the applicability of the monitoring approach under representative field conditions. However, extrapolating these results to the entire heliostat population would require validation across a larger, more spatially distributed sample.

4.5. ACMS Cost Relative to Heliostat Cost and Market Perspective

A rough cost comparison between the proposed cost-efficient ACMS and a conventional industrial-grade sensor and datalogger setup is performed:

- ACMS: 3-axis acceleration sensor, Hall-effect sensor, analogue signal conditioning, Arduino GIGA microcontroller approximately 105 € vs.
- Conventional industrial-grade setup: PC oscilloscope, current clamps, industrial-grade vibration measurement system with sensor and data logger approximately 7400 €.

This yields a cost reduction factor of roughly $70 \approx \frac{7400\,€}{105\,€}$ for the instrumentation of a single heliostat. All prices correspond to typical market values in Germany during the second half of 2025. In both cases, an additional measurement computer is required for measurement control and data acquisition. Although the values presented here should be regarded as indicative order-of-magnitude estimates rather than the results of a detailed economic analysis, the cost difference of a factor of 70 remains substantial. This is particularly relevant in utility-scale fields with 10^3–10^5 heliostats, where scalability is essential.

To put these calculated costs into context, literature studies [53–55] report estimated or target heliostat costs in the range of approximately 75 USD m^{-2} to 127 USD m^{-2} of reflective heliostat area resulting in total costs of roughly 500 € to 880 € per heliostat. (For this brief calculation, an exchange rate of 1 USD $\approx$ 0.86 € and about 8 m^2 per heliostat as in the heliostat field of the STJ [49] has been assumed.) Therefore, under these simplified assumptions, the hardware costs of the ACMS of 105 € correspond to approximately 11–21% of the total heliostat costs. While not a full economic assessment, this estimate suggests that, when monitoring large numbers of heliostats, monitoring costs at this level become a very significant factor. However, future developments involving highly integrated, industrially manufactured sensor modules that combine sensing, signal conditioning and microcontroller functionality on a single board may further reduce costs.

Looking towards future developments, solar tower technology currently represents a comparatively small but well-established segment of CST deployment [56]. As of 2023, approximately 1802 MW of solar tower capacity has been installed worldwide across 34 projects, with a median solar field area of around 208,240 m^2 per plant [57]. Meanwhile, the Chinese market is experiencing rapid growth, with approximately 6.7 GW of solar tower capacity reported to be under development or planned as of 2025 [58]. In such large-scale deployments, cost-efficient solutions become increasingly essential for the scalable monitoring of HDUs in heliostat fields.

5. Conclusions and Outlook

5.1. Summary of This Work

This study presents the conception, development, and experimental validation of an ACMS for HDUs. Existing research on heliostat O&M has so far mainly addressed optical performance aspects, wind-induced effects as well as tracking and calibration methods. However, experimental investigations of monitoring concepts for HDUs remain largely absent in the literature. The experimental results obtained during the measurement campaign conducted at the STJ demonstrate that the proposed ACMS enables the identification of emerging deviations in the operational behaviour of the HDUs. Potential

wind-induced effects, which can influence heliostat behaviour in general, are assessed during the measurements through simultaneous wind monitoring and correlation analyses. There is no indication of a dominant influence on the observed heliostat behaviour. Detecting such not wind-induced deviations from baseline HDU behaviour at an early stage allows their potential causes to be investigated systematically and can support timely maintenance decisions.

All in all, this promotes the reliable and economically efficient operation of large heliostat fields as part of critical energy infrastructure. While developed and validated for HDUs, the proposed monitoring methodology may also be transferable to other electromechanical systems in industrial condition monitoring contexts.

5.2. Further Evaluation Requirements and Current Limitations

While this study demonstrates the feasibility of the ACMS approach, further systematic validation is required to assess the robustness and long-term reliability of the developed ACMS during extended multi-month or multi-year field operations and outdoor exposure. Factors such as environmental influences, sensor ageing, cable degradation, potential long-term signal drift, as well as practically unavoidable installation-related variations in sensor placement, orientation, and coupling to the HDU may affect measurement stability and therefore require further investigation. Additionally, targeted physical inspections and root-cause analyses of HDUs exhibiting abnormal operational behaviour would provide valuable information for linking deviations in the recorded measurement data to specific underlying failure mechanisms.

Additional aspects to be addressed in future studies regarding the deployment of the ACMS include automated sensor calibration, robust communication, data integrity, cybersecurity and integration into plant-level O&M infrastructures. Moreover, while the present work demonstrates the detectability of condition-sensitive changes in operational sensor data, it does not yet provide a validated degradation model or a prediction of the remaining useful life (RUL), nor a prescriptive maintenance (cf. Figure 2) concept for the HDUs.

Furthermore, a relevant next step would be to investigate how the sensor and data acquisition requirements presented in this work can be reduced while ensuring that the necessary diagnostic information for the HDUs can still be extracted from the recorded operational data. This reduction may involve the type and number of sensors, their placement, sampling rates, and the number and selection of instrumented heliostats. Redundancy within and between the different elements of the measurement strategy should also be considered. For instance, there may be similarities between vibration measurements taken along the three orthogonal axes, or between vibration and magnetic flux density signals.

5.3. Future Experimental Work

A future measurement campaign at the STJ may extend the present study by investigating both field-wide scalability options for the proposed monitoring concept, as well as the behaviour of HDUs when subjected to controlled artificial ageing and deliberate stress. Generating fault-related data on demand reduces the dependence on rare, naturally occurring operational failures, enabling a more systematic analysis of stress–response relationships in HDUs. Moreover, future work could expand the measurement architecture to include wireless communication, battery-powered operation, local data storage, and edge computing capabilities.

6. Patents

The methods described in this study are subject of a pending German patent application filed with the German Patent and Trade Mark Office on 6 July 2026 entitled "Verfahren zur Zustandsbestimmung einer Antriebsvorrichtung eines Heliostaten" (Application no. DE 10 2026 127 943.0).

Author Contributions: Conceptualisation, D.S.; Methodology, D.S. and S.N.H.; Software, D.S. and S.N.H.; Validation, D.S. and S.N.H.; Formal Analysis, D.S. and S.N.H.; Investigation, D.S. and S.N.H.; Resources, D.M.Q.; Data Curation, D.S. and S.N.H.; Writing—Original Draft Preparation, D.S.; Writing—Review and Editing, D.S. and B.K.; Visualisation, D.S. and S.N.H.; Supervision, D.M.Q., M.R., B.K. and R.P.-P.; Project Administration, D.S.; Funding Acquisition, D.M.Q., M.R., B.K. and R.P.-P. All authors have read and agreed to the published version of the manuscript.

Funding: This research received no external funding.

Data Availability Statement: The original data presented in this study are openly available on Zenodo [50].

Acknowledgments: The authors gratefully acknowledge the support of the technical and scientific staff at the STJ, in particular Oliver Kaufhold and Marcel Sibum, for their assistance during the measurement campaign. During the preparation of this work, the authors used the language model ChatGPT-5 (OpenAI), as well as the free versions of DeepL Translate and DeepL Write (DeepL SE), to assist with refining the clarity, conciseness, structure, and linguistic quality of the manuscript; LaTeX-based formatting, including the preparation and arrangement of figures, tables, and captions; and Python-based data processing and visualisation. The latter included the provision and revision of example code, clarification of library functionalities and data-processing procedures, and assistance with code refactoring and documentation. The authors have reviewed and edited the output and take full responsibility for the content of this publication.

Conflicts of Interest: The authors declare no conflicts of interest.

Abbreviations

The following abbreviations are used in this manuscript:

HDU	Heliostat drive unit
O&M	Operation and maintenance
ACMS	Arduino-based condition monitoring system
STJ	DLR solar tower research facility in Jülich, Germany
CST	Concentrating solar technologies
MEMS	Micro-Electromechanical System
PV	Photovoltaics
ADC	Analogue-to-digital converter
RMSE	Root mean squared error
FFT	Fast Fourier transform
STFT	Short-Time Fourier transform

Appendix A. Additional Information on the Measurement System

Appendix A.1. Analogue Signal Conditioning

The analogue signal conditioning stage comprises a first-order RC high-pass filter, a voltage divider that introduces a DC offset, and a non-inverting amplifier. The high-pass filter suppresses low-frequency components, while the offset shifts the signal into the usable ADC input range. The normalised, frequency-dependent magnitude response $|H(f)|$ of the first-order high-pass filter is given by

$$|H(f)| = \frac{f/f_c}{\sqrt{1+(f/f_c)^2}}, \tag{A1}$$

where f is the signal frequency and f_c the cutoff frequency. For $f \ll f_c$, $|H(f)| \approx f/f_c \to 0$, whereas for $f \gg f_c$, $|H(f)| \to 1$. Hence, static and slowly varying signal components are strongly attenuated, while higher-frequency signal components are retained. The non-inverting amplifier increases the signal amplitude and thereby improves the effective resolution of the subsequent digitisation.

The circuit parameters are determined based on the experimental requirements and are validated through preliminary measurements. Although a theoretical maximum gain of approximately $V_{max} \approx 33$ is possible, a nominal gain of $V_{chosen} = 11.5$ was selected to avoid saturation in the event of abnormal vibration amplitudes. The experimentally measured gain is $V_{measured} = 11.6$, which is consistent with V_{chosen} when considering the expected tolerances of the analogue components and the Arduino ADC. The cutoff frequency f_c was calculated as $f_c = 15.9\,\text{Hz}$ and experimentally determined as approximately 16.0 Hz, confirming the intended filter behaviour.

Experimental verification has confirmed that the signal conditioning stage both exhibits a linear response within the relevant measurement range and does not introduce significant additional measurement errors. Moreover, the amplification improves the signal-to-noise ratio of the recorded measurements.

Appendix A.2. ADC Resolution and Measurement Uncertainty

The ADCs of the STM32H747XI microcontroller used in this study are configured with a resolution of 16 bit [59]. For the analogue input range considered here, defined by $U_{ref-} = 0.0\,\text{V}$ and $U_{ref+} = 3.3\,\text{V}$, the ideal ADC voltage step size ΔU is given by $\Delta U = (U_{ref+} - U_{ref-})/2^{16}$, resulting in $\Delta U \approx 50.4\,\mu\text{V}$. This value represents the nominal quantisation resolution and should not be interpreted as the absolute measurement accuracy. The microcontroller datasheet specifies a tolerance of 10 LSB for 16-bit ADC operation. This corresponds to an ADC-level tolerance of approximately $10 \times 50.4\,\mu\text{V} \approx 0.50\,\text{mV}$.

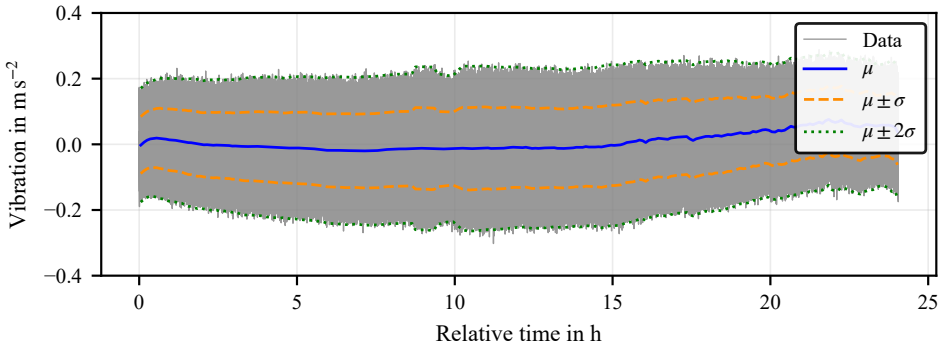
The overall measurement uncertainty is affected by several factors, including the reference-voltage stability, ADC offset and gain errors, sensor accuracy, temperature drift, and electromagnetic interference. To improve measurement precision, the measurement value of each analogue sensor was obtained by averaging $m = 8$ consecutive ADC readings. For predominantly uncorrelated random noise, this reduces the standard deviation of the random noise component by $1/\sqrt{m} = 1/\sqrt{8} \approx 0.354$. Preliminary experiments confirmed that this procedure stabilises the analogue readings and that the additional repeated ADC reading operations did not constitute a computational bottleneck for the chosen configuration (cf. Equation (1)). While this averaging reduces random fluctuations, it does not compensate for systematic uncertainty contributions such as calibration errors, reference-voltage deviations, ADC non-linearities, or a potential sensor bias.

However, the uncertainty of the overall measurement chain is considered acceptable for the objectives of this study. The proposed monitoring approach focuses on identifying deviations between the expected baseline behaviour and the actual operational behaviour as indicators of emerging anomalies or maintenance requirements, rather than on highly accurate absolute measurement values.

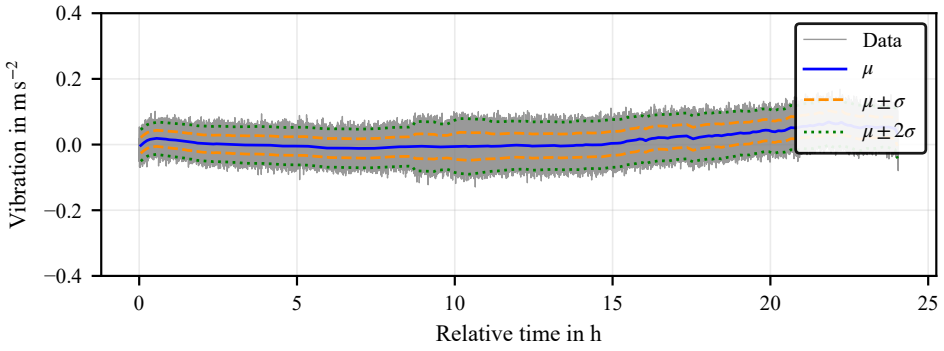
Appendix B. Additional Measurement Data

24-h-Stability Measurements

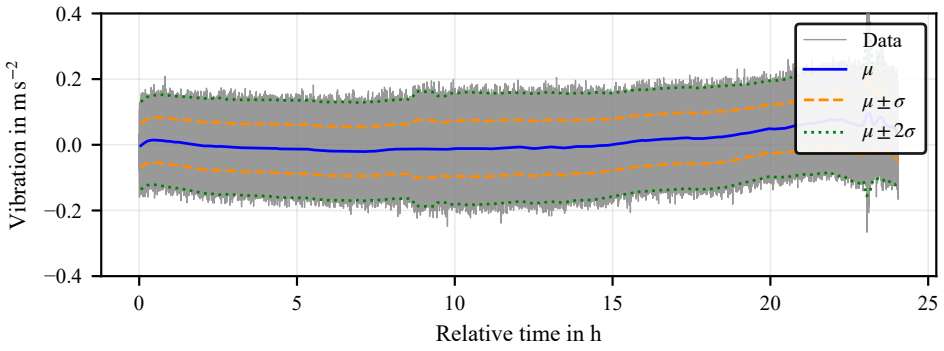
The following two figures (Figures A1 and A2) present the 24-h-stability measurements of the vibration and the magnetic flux density.



(**a**)



(**b**)



(**c**)

Figure A1. 24-h-stability vibration measurements at Axis 1 in the (**a**) Transversal (North–South)-, (**b**) Transversal (East–West)-, and (**c**) Axial (z)—directions. The data are shown together with the interval-wise mean μ and the corresponding $\mu \pm \sigma$ and $\mu \pm 2\sigma$ bounds, with all statistics calculated separately for consecutive six-minute intervals.

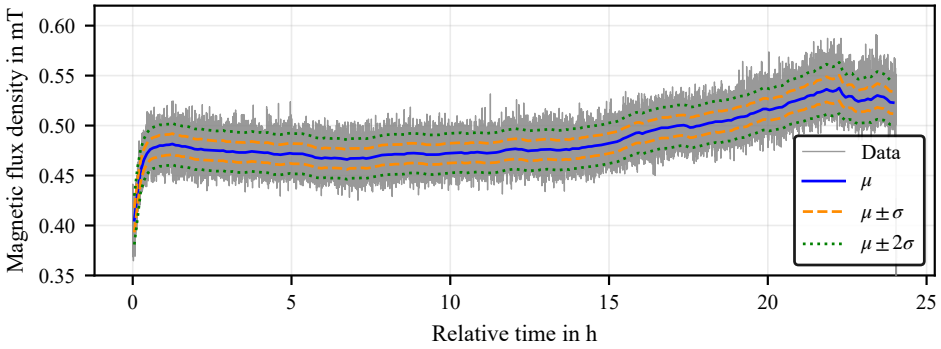


Figure A2. 24-h-stability magnetic flux density measurement at Axis 1 in transversal (North-South) direction. The data are shown together with the interval-wise mean μ and the corresponding $\mu \pm \sigma$ and $\mu \pm 2\sigma$ bounds, with all statistics calculated separately for consecutive six-minute intervals.

Table A1. Summary of the 24-h-stability assessment: Data availability is the ratio of finite acquired to nominally expected samples. Data gaps are intervals between consecutive samples exceeding 1.5 times the nominal sampling interval $T_{\text{sample}} = 1/f_{\text{chosen}}$ cf. Equation (1). Max$[\Delta T_{\text{sample}}]$ denotes the maximum observed interval. For further analysis, data are divided into consecutive six-minute intervals (i.e., 10 intervals per hour). Threshold exceedances denote the fraction of samples lying outside the interval-specific $\mu \pm 2\sigma$, $\mu \pm 3\sigma$, and $\mu \pm 4\sigma$ bounds. Linear drift is determined from a linear fit to the interval means, and the σ-normed drift expresses the absolute linear drift rate per hour in units of the average interval standard deviation.

Metric	**Vibration**			**Magnetic Field**
	Transversal (N–S)	**Transversal (E–W)**	**Axial (z)**	**Transversal (N–S)**
Data continuity				
Availability (%)		99.92		
Data gaps		840		
Max$[\Delta T_{\text{sample}}]$ (ms)		14.669		
Threshold exceedances				
Data $> 2\sigma$ (%)	0.4155	3.4805	2.1830	4.8840
Data $> 3\sigma$ (10^{-3}%)	0.03	20.73	2.65	572.47
Data $> 4\sigma$ (10^{-4}%)	0.00	0.10	0.00	518.00
Temporal drift				
Linear drift rate ($10^{-3}\,\text{h}^{-1}$)	$2.84\,\text{m}\,\text{s}^{-2}$	$2.49\,\text{m}\,\text{s}^{-2}$	$3.21\,\text{m}\,\text{s}^{-2}$	2.71 mT
σ-normed drift rate (%$\,\text{h}^{-1}$)	2.57	7.61	4.09	26.18

Appendix C. Additional Analyses

Electrical Interpretation of the Series-Resistance Experiment

To support the physical interpretation of the controlled motor-phase resistance variation discussed in Section 4.2 (cf. Figure 12), this appendix subsection provides a first-order electrical analysis. It examines how R affects the motor-phase currents and consequently the magnetic field generated by the motor windings.

Preliminary measurements using current clamps (as also used, e.g., in Section 4.1.4) show that the additional resistance $R = R_{\text{external}}$ affects both the current amplitudes $\hat{I}_k$ and the phase relationship

$$\Delta\varphi = |\varphi_1 - \varphi_2| \tag{A2}$$

between the two motor-phase currents

$$I_k(t) = \hat{I}_k \sin(\omega t + \varphi_k), \qquad k \in \{1, 2\}. \tag{A3}$$

As a first-order interpretation, the affected motor phase can be approximated as an inductive RL load with

$$Z = R_{\text{total}} + j\omega L, \tag{A4}$$

where

$$R_{\text{total}} = R_{\text{winding}} + R_{\text{external}}. \tag{A5}$$

Here, L denotes the inductance of the affected motor phase and ω the angular frequency of the applied electrical excitation. For a sinusoidal phase voltage with amplitude $\hat{V}$, the corresponding current amplitude is given by

$$\hat{I} = \frac{\hat{V}}{\sqrt{R_{\text{total}}^2 + (\omega L)^2}}. \tag{A6}$$

The phase angle of the corresponding complex impedance Z is

$$\theta_Z = \arctan\left(\frac{\omega L}{R_{\text{total}}}\right). \tag{A7}$$

For a voltage reference phase of zero, the current lags the applied voltage by this angle, i.e., its phase contribution due to the RL impedance is $-\theta_Z$.

Accordingly, increasing $R = R_{\text{external}}$, as it is done during the experiments, has two relevant effects. First, it reduces the current amplitude $\hat{I}$ according to Equation (A6). Second, it changes the impedance phase angle θ_Z according to Equation (A7) and thereby modifies the current phase response and, consequently, the relative phase position $\Delta\varphi$ between the two motor-phase currents.

The latter effect is particularly relevant because smooth motor operation with low vibration excitation requires both phase currents $I_1(t)$ and $I_2(t)$ to maintain their intended and temporally stable phase relationship. For an ideal two-phase motor with equal current amplitudes and orthogonal phase currents, i.e., $\Delta\varphi = \pi/2$, the current-vector trajectory is circular. This corresponds to a nearly uniform rotation of the electromagnetic field and thus smooth torque generation. However, an amplitude imbalance and/or a deviation from an orthogonal phase relationship results in an elliptical trajectory in the Lissajous representation, indicating a non-uniform field rotation.

Such a distorted field rotation can result in periodic variations in the electromagnetic torque, i.e., torque ripple, which may excite the motor, gearbox, and drive unit structure at characteristic frequencies, as can be seen in Figure 12. Therefore, the R-dependent increase in vibration peaks can be interpreted as a possible consequence of phase-current distortion and the resulting torque ripple.

References

1. Steinberg, D.; Huestegge, S.N.; Maldonado Quinto, D.; Röger, M.; Kölsch, B.; Pitz-Paal, R. Cost-Efficient Prognostics Framework for Heliostat Drive Units. *Proc. Eur. Conf. PHM Soc.* **2026**, *9*, 1–17. [CrossRef]
2. Stengler, J.; Bülow, M.; Pitz-Paal, R. Concentrating solar technologies for low-carbon energy. *Nat. Rev. Clean Technol.* **2025**, *1*, 719–733. [CrossRef]
3. Pfahl, A.; Coventry, J.; Röger, M.; Wolfertstetter, F.; Vásquez-Arango, J.F.; Gross, F.; Arjomandi, M.; Schwarzbözl, P.; Geiger, M.; Liedke, P. Progress in heliostat development. *Sol. Energy* **2017**, *152*, 3–37. [CrossRef]
4. Osman, M.; Qureshi, I. Review of photovoltaic and concentrated solar technologies including their performance, reliability, efficiency and storage. *Results Eng.* **2025**, *25*, 104424. [CrossRef]
5. Zio, E. Prognostics and Health Management (PHM): Where are we and where do we (need to) go in theory and practice. *Reliab. Eng. Syst. Saf.* **2022**, *218*, 108119. [CrossRef]

6. Calabrese, F.; Regattieri, A.; Bortolini, M.; Gamberi, M.; Pilati, F. Predictive Maintenance: A Novel Framework for a Data-Driven, Semi-Supervised, and Partially Online Prognostic Health Management Application in Industries. *Appl. Sci.* **2021**, *11*, 3380. [CrossRef]
7. Ali, A.; Abdelhadi, A. Condition-Based Monitoring and Maintenance: State of the Art Review. *Appl. Sci.* **2022**, *12*, 688. [CrossRef]
8. Cannavacciuolo, L.; Ferraro, G.; Ponsiglione, C.; Primario, S.; Quinto, I. Technological innovation-enabling industry 4.0 paradigm: A systematic literature review. *Technovation* **2023**, *124*, 102733. [CrossRef]
9. Achouch, M.; Dimitrova, M.; Ziane, K.; Sattarpanah Karganroudi, S.; Dhouib, R.; Ibrahim, H.; Adda, M. On Predictive Maintenance in Industry 4.0: Overview, Models, and Challenges. *Appl. Sci.* **2022**, *12*, 8081. [CrossRef]
10. Aoun, A.; Ilinca, A.; Ghandour, M.; Ibrahim, H. A review of Industry 4.0 characteristics and challenges, with potential improvements using blockchain technology. *Comput. Ind. Eng.* **2021**, *162*, 107746. [CrossRef]
11. Surucu, O.; Gadsden, S.A.; Yawney, J. Condition Monitoring using Machine Learning: A Review of Theory, Applications, and Recent Advances. *Expert Syst. Appl.* **2023**, *221*, 119738. [CrossRef]
12. Er-Ratby, M.; Kobi, A.; Sadraoui, Y.; Kadiri, M.S. The Impact of Predictive Maintenance on the Performance of Industrial Enterprises. *SN Comput. Sci.* **2025**, *6*, 73. [CrossRef]
13. Grand View Research. Machine Condition Monitoring Market Report: Industry Analysis and Forecast. 2026. Available online: https://www.grandviewresearch.com/industry-analysis/machine-condition-monitoring-market-report (accessed on 28 July 2026).
14. Teixeira, H.N.; Lopes, I.; Braga, A.C. Condition-based maintenance implementation: A literature review. *Procedia Manuf.* **2020**, *51*, 228–235. [CrossRef]
15. Jasiulewicz-Kaczmarek, M.; Legutko, S.; Kluk, P. Maintenance 4.0 technologies—New opportunities for sustainability driven maintenance. *Manag. Prod. Eng. Rev.* **2020**, *11*, 74–87. [CrossRef]
16. Roehrich, G.; Raffaele, D. Predictive maintenance: Advanced fault classification. *Int. J. Syst. Assur. Eng. Manag.* **2024**. [CrossRef]
17. Yazdi, M. *Advances in Computational Mathematics for Industrial System Reliability and Maintainability*, 1st ed.; Springer Series in Reliability Engineering; Springer: Cham, Switzerland, 2024; pp. XIV–190. [CrossRef]
18. Ansari, F.; Glawar, R.; Nemeth, T. PriMa: A prescriptive maintenance model for cyber-physical production systems. *Int. J. Comput. Integr. Manuf.* **2019**, *32*, 482–503. [CrossRef]
19. Zonta, T.; da Costa, C.A.; da Rosa Righi, R.; de Lima, M.J.; da Trindade, E.S.; Li, G.P. Predictive maintenance in the Industry 4.0: A systematic literature review. *Comput. Ind. Eng.* **2020**, *150*, 106889. [CrossRef]
20. Sarver, T.; Al-Qaraghuli, A.; Kazmerski, L.L. A comprehensive review of the impact of dust on the use of solar energy: History, investigations, results, literature, and mitigation approaches. *Renew. Sustain. Energy Rev.* **2013**, *22*, 698–733. [CrossRef]
21. Ilse, K.; Micheli, L.; Figgis, B.W.; Lange, K.; Daßler, D.; Hanifi, H.; Wolfertstetter, F.; Naumann, V.; Hagendorf, C.; Gottschalg, R.; et al. Techno-Economic Assessment of Soiling Losses and Mitigation Strategies for Solar Power Generation. *Joule* **2019**, *3*, 2303–2321. [CrossRef]
22. Wette, J.; Sutter, F.; Enrique-Orts, R.; Pérez-García, M.; Sánchez-Moreno, R.; Fernández-García, A. Soiling of solar-field heliostats during operation in concentrating solar thermal plants. *Results Eng.* **2025**, *28*, 107890. [CrossRef]
23. Ashley, T.; Carrizosa, E.; Fernández-Cara, E. Heliostat field cleaning scheduling for Solar Power Tower plants: A heuristic approach. *Appl. Energy* **2019**, *235*, 653–660. [CrossRef]
24. Emes, M.; Jafari, A.; Pfahl, A.; Coventry, J.; Arjomandi, M. A review of static and dynamic heliostat wind loads. *Sol. Energy* **2021**, *225*, 60–82. [CrossRef]
25. Todd Griffith, D.; Moya, A.C.; Ho, C.K.; Hunter, P.S. Structural Dynamics Testing and Analysis for Design Evaluation and Monitoring of Heliostats. *J. Sol. Energy Eng.* **2014**, *137*, 021010. [CrossRef]
26. Blackmon, J.B. Heliostat drive unit design considerations—Site wind load effects on projected fatigue life and safety factor. *Sol. Energy* **2014**, *105*, 170–180. [CrossRef]
27. Bakhshipour, S.; Emes, M.J.; Arjomandi, M. Local pressure distributions on a heliostat facet and its Strouhal number in turbulent flow. *Sol. Energy* **2026**, *307*, 114267. [CrossRef]
28. Sattler, J.C.; Röger, M.; Schwarzbözl, P.; Buck, R.; Macke, A.; Raeder, C.; Göttsche, J. Review of heliostat calibration and tracking control methods. *Sol. Energy* **2020**, *207*, 110–132. [CrossRef]
29. Pargmann, M.; Maldonado Quinto, D.; Schwarzbözl, P.; Pitz-Paal, R. High accuracy data-driven heliostat calibration and state prediction with pretrained deep neural networks. *Sol. Energy* **2021**, *218*, 48–56. [CrossRef]
30. Moreno-Cruz, I.; Paredes-Orta, C.; Martell-Chávez, F.; Salgado-Tránsito, I. Heliostat drift prediction model to improve heliostat position control in solar fields. *Sol. Energy* **2025**, *289*, 113323. [CrossRef]
31. Schnerring, A.; Röger, M.; Winter, A.; Broda, R.; Nieslony, M.; Algner, N.; Kölsch, B.; Pitz-Paal, R. Airborne real-time solar concentrator orientation estimation for heliostat fine calibration. *Sol. Energy* **2026**, *316*, 114823. [CrossRef]
32. Tian, M.; Chidambaranathan, K.; Rafique, M.Z.E.; Desai, N.; Bai, J.; Brost, R.; Small, D.; Novick, D.; Yellowhair, J.; Yao, Y. Heliostat optical error inspection with polarimetric imaging drone. *Sol. Energy* **2026**, *304*, 114185. [CrossRef]

33. Jundi, Z.S.; Al-Waeli, A.H.; Switzner, N.T. A systematic review of low-cost photovoltaic monitoring Systems: Technologies, challenges, and opportunities. *Renew. Sustain. Energy Rev.* **2026**, *226*, 116417. [CrossRef]
34. Soto-Ocampo, C.R.; Mera, J.M.; Cano-Moreno, J.D.; Garcia-Bernardo, J.L. Low-Cost, High-Frequency, Data Acquisition System for Condition Monitoring of Rotating Machinery through Vibration Analysis-Case Study. *Sensors* **2020**, *20*, 3493. [CrossRef] [PubMed]
35. Huang, C.; Bu, S.; Lee, H.H.; Chan, C.H.; Kong, S.W.; Yung, W.K. Prognostics and health management for predictive maintenance: A review. *J. Manuf. Syst.* **2024**, *75*, 78–101. [CrossRef]
36. Failing, J.M.; Abellán-Nebot, J.V.; Benavent Nácher, S.; Rosado Castellano, P.; Romero Subirón, F. A Tool Condition Monitoring System Based on Low-Cost Sensors and an IoT Platform for Rapid Deployment. *Processes* **2023**, *11*, 668. [CrossRef]
37. Mykoniatis, K. A Real-Time Condition Monitoring and Maintenance Management System for Low Voltage Industrial Motors Using Internet-of-Things. *Procedia Manuf.* **2020**, *42*, 450–456. [CrossRef]
38. Villacorta, J.J.; del Val, L.; Martínez, R.D.; Balmori, J.A.; Magdaleno, Á.; López, G.; Izquierdo, A.; Lorenzana, A.; Basterra, L.A. Design and Validation of a Scalable, Reconfigurable and Low-Cost Structural Health Monitoring System. *Sensors* **2021**, *21*, 648. [CrossRef] [PubMed]
39. Binali, R.; Demirpolat, H.; Kuntoğlu, M.; Makhesana, M.; Yaghoubi, S.; Sayın Kul, B. A Comprehensive Review on Low-Cost MEMS Accelerometers for Vibration Measurement: Types, Novel Designs, Performance Evaluation, and Applications. *J. Mol. Eng. Mater.* **2024**, *12*, 2430002. [CrossRef]
40. Kolok, P.; Hodoň, M.; Ševčík, P.; Hotz, L.; Remy, N. Low-Cost IoT-Based Predictive Maintenance Using Vibration. *Sensors* **2025**, *25*, 6610. [CrossRef] [PubMed]
41. Villarroel, A.; Zurita, G.; Velarde, R. Development of a Low-Cost Vibration Measurement System for Industrial Applications. *Machines* **2019**, *7*, 12. [CrossRef]
42. Hasibuzzaman, M.; Shufian, A.; Shefa, R.; Raihan, R.; Ghosh, J.; Sarker, A. Vibration Measurement & Analysis Using Arduino-Based Accelerometer. In *Proceedings of the IEEE Region 10 Symposium (TENSYMP)*; IEEE: Piscataway, NJ, USA, 2020. [CrossRef]
43. Jakobsen, M.O. Low cost MEMS accelerometer and microphone based condition monitoring sensor, with LoRa and Bluetooth Low Energy radio. *HardwareX* **2024**, *18*, e00525. [CrossRef] [PubMed]
44. Komarizadehasl, S.; Mobaraki, B.; Ma, H.; Lozano-Galant, J.A.; Turmo, J. Development of a Low-Cost System for the Accurate Measurement of Structural Vibrations. *Sensors* **2021**, *21*, 6191. [CrossRef] [PubMed]
45. Tiboni, M.; Remino, C.; Bussola, R.; Amici, C. A Review on Vibration-Based Condition Monitoring of Rotating Machinery. *Appl. Sci.* **2022**, *12*, 972. [CrossRef]
46. Nkinyam, C.M.; Ujah, C.O.; Asadu, C.O.; Anyaka, B.; Olubambi, P.A. Development of a low-cost monitoring device for solar electric (PV) system using internet of things (IoT). *Results Eng.* **2025**, *28*, 107324. [CrossRef]
47. Hossain, M.S.; Ali Bashir, M.B.; Akter, K. Design a low-cost solar PV data logger and assess the application and accuracy with off-grid monocrystalline panels. *Measurement* **2026**, *258*, 119176. [CrossRef]
48. Arduino. Arduino GIGA R1 WiFi User Manual. Available online: https://docs.arduino.cc/resources/datasheets/ABX00063-datasheet.pdf (accessed on 24 July 2026).
49. Göhring, F.; Kaufhold, O.; Quinto, D.M.; Sibum, M.; Wirger, M. Operational experiences with the heliostat field at the Juelich solar towers. In *Proceedings of the Advances in Solar Energy: Heliostat Systems Design, Implementation, and Operation*; Zhu, G., Röger, M., Wang, Z., Eds.; International Society for Optics and Photonics (SPIE): San Diego, CA, USA, 2023; Volume 12671, p. 1267109. [CrossRef]
50. Steinberg, D.; Huestegge, S.N.; Maldonado Quinto, D.; Röger, M.; Kölsch, B.; Pitz-Paal, R. Experimental Data of the Field Validation of an Arduino-Based Condition Monitoring System for Heliostat Drive Units. *Zenodo* **2026**. [CrossRef]
51. Luo, H.; Li, Z.; Xiong, Q. Study on wind-induced fatigue of heliostat based on artificial neural network. *J. Wind Eng. Ind. Aerodyn.* **2021**, *217*, 104750. [CrossRef]
52. Paulus, L.; Hanrieder, N.; Plessing, T.; Gonzalez Rodriguez, S.; Gramitzky, K.; Deuerlein, L.; Kühn, P.; Fernández-Reche, J.; Zarzalejo, L.F.; Röger, M.; et al. Heliostat Tracking Influence on Wind Pattern within a Real-Scale Heliostat Field. In Proceedings of the SolarPACES Conference 2024, Rome, Italy, 8–11 October 2024. Available online: https://elib.dlr.de/207716/ (accessed on 17 September 2026).
53. Pfahl, A.; Randt, M.; Holze, C.; Unterschütz, S. Autonomous light-weight heliostat with rim drives. *Sol. Energy* **2013**, *92*, 230–240. [CrossRef]
54. Blackmon, J.B. Parametric determination of heliostat minimum cost per unit area. *Sol. Energy* **2013**, *97*, 342–349. [CrossRef]
55. Kurup, P.; Akar, S.; Glynn, S.; Augustine, C.; Davenport, P. *Cost Update: Commercial and Advanced Heliostat Collectors*; Technical Report NREL/TP-7A40-80482; National Renewable Energy Laboratory (NREL): Golden, CO, USA, 2022. [CrossRef]
56. International Renewable Energy Agency (IRENA). *Renewable Energy Statistics 2026*; Technical Report; International Renewable Energy Agency: Abu Dhabi, United Arab Emirates, 2026.
57. Alami, A.H.; Olabi, A.; Mdallal, A.; Rezk, A.; Radwan, A.; Rahman, S.M.A.; Shah, S.K.; Abdelkareem, M.A. Concentrating solar power (CSP) technologies: Status and analysis. *Int. J. Thermofluids* **2023**, *18*, 100340. [CrossRef]

58. Lynch, B.; Metghalchi, H.; Levendis, Y. Concentrating Solar Thermal Power in China: 2025 Review and Outlook. *ASME Open J. Eng.* **2025**, *4*, 040807. [CrossRef]
59. STMicroelectronics. STM32H747xI/G Datasheet. Available online: https://www.st.com/resource/en/datasheet/stm32h747ai.pdf (accessed on 24 July 2026).

Disclaimer/Publisher's Note: The statements, opinions and data contained in all publications are solely those of the individual author(s) and contributor(s) and not of MDPI and/or the editor(s). MDPI and/or the editor(s) disclaim responsibility for any injury to people or property resulting from any ideas, methods, instructions or products referred to in the content.